

# The Microlensing Event Rate and Optical Depth Toward the Galactic Bulge from MOA-II

T. Sumi<sup>1</sup>, D.P. Bennett<sup>2</sup>, I.A. Bond<sup>3</sup>, F. Abe<sup>4</sup>, C.S. Botzler<sup>5</sup>, A. Fukui<sup>6</sup>, K. Furusawa<sup>4</sup>,  
Y. Itow<sup>4</sup>, C.H. Ling<sup>3</sup>, K. Masuda<sup>4</sup>, Y. Matsubara<sup>4</sup>, Y. Muraki<sup>4</sup>, K. Ohnishi<sup>7</sup>,  
N. Rattenbury<sup>5</sup>, To. Saito<sup>8</sup>, D.J. Sullivan<sup>9</sup>, D. Suzuki<sup>1</sup>, W.L. Sweatman<sup>3</sup>, P.,J. Tristram<sup>10</sup>,  
K. Wada<sup>1</sup>, P.C.M. Yock<sup>5</sup>  
(The MOA Collaboratoin)

## ABSTRACT

We present measurements of the microlensing optical depth and event rate toward the Galactic Bulge based on two years of the MOA-II survey. This sample contains  $\sim 1000$  microlensing events, with an Einstein Radius crossing time of  $t_E \leq 200$  days in 22 bulge fields covering  $\sim 42 \text{ deg}^2$  between  $-5^\circ < l < 10^\circ$  and  $-7^\circ < b < -1^\circ$ . Our event rate and optical depth analysis uses 474 events with well defined microlensing parameters. In the central fields with  $|l| < 5^\circ$ , we find an event rates of  $\Gamma = [2.39 \pm 1.1]e^{[0.60 \pm 0.05](3-|b|)} \times 10^{-5} \text{ star}^{-1} \text{ yr}^{-1}$  and an optical depth (for events with  $t_E \leq 200$  days) of  $\tau_{200} = [2.35 \pm 0.18]e^{[0.51 \pm 0.07](3-|b|)} \times 10^{-6}$

---

<sup>1</sup>Department of Earth and Space Science, Graduate School of Science, Osaka University, Toyonaka, Osaka 560-0043, Japan,  
e-mail: sumi@ess.sci.osaka-u.ac.jp

<sup>2</sup>Department of Physics, University of Notre Dame, Notre Dame, IN 46556, USA; bennett@nd.edu

<sup>3</sup>Institute of Information and Mathematical Sciences, Massey University, Private Bag 102-904, North Shore Mail Centre, Auckland, New Zealand; i.a.bond,c.h.ling,w.sweatman@massey.ac.nz

<sup>4</sup>Solar-Terrestrial Environment Laboratory, Nagoya University, Nagoya 464-8601, Japan; abe,furusawa,itow,kmasuda,ymatsu@stelab.nagoya-u.ac.jp

<sup>5</sup>Department of Physics, University of Auckland, Private Bag 92019, Auckland, New Zealand; c.botzler,p.yock@auckland.ac.nz

<sup>6</sup>Okayama Astrophysical Observatory, National Astronomical Observatory of Japan, 3037-5 Honjo, Kamogata, Asakuchi, Okayama 719-0232, Japan

<sup>7</sup>Nagano National College of Technology, Nagano 381-8550, Japan

<sup>8</sup>Tokyo Metropolitan College of Aeronautics, Tokyo 116-8523, Japan

<sup>9</sup>School of Chemical and Physical Sciences, Victoria University, Wellington, New Zealand

<sup>10</sup>Mt. John University Observatory, P.O. Box 56, Lake Tekapo 8770, New Zealand

for the 427 events using all sources brighter than  $I_s \leq 20$  mag. The distribution of observed fields is centered at  $(l, b) = (0.^{\circ}38, -3.^{\circ}72)$ . We find that the event rate is maximized at low latitudes and a longitude of  $l \approx 1^{\circ}$ . For the 111 events in  $3.2 \text{ deg}^2$  of the central Galactic Bulge at  $|b| \leq 3^{\circ}.0$  and  $0^{\circ}.0 \leq l \leq 2^{\circ}.0$ , centered at  $(l, b) = (0.^{\circ}97, -2.^{\circ}26)$ , we find  $\Gamma = 4.57^{+0.51}_{-0.46} \times 10^{-5} \text{ star}^{-1} \text{ yr}^{-1}$  and  $\tau_{200} = 3.64^{+0.51}_{-0.45} \times 10^{-6}$ . We also consider a Red Clump Giant (RCG) star sample with  $I_s < 17.5$ , and we find that the event rate for the RCG sample is slightly lower than but consistent with the all-source event rate. The main difference is the lack of long duration events in the RCG sample, due to a known selection effect. Our results are consistent with previous optical depth measurements, but they are somewhat lower than previous all-source measurements and slightly higher than previous RCG optical depth measurements. This suggests that the previously observed difference in optical depth measurements between all-source and RCG samples may be largely due to statistical fluctuations. These event rate measurements towards the central galactic bulge are necessary to predict the microlensing event rate and to optimize the survey fields in the future space mission such as WFIRST.

*Subject headings:* gravitational lensing – Galaxy: bulge – stars: variables: other

## 1. Introduction

The gravitational microlensing surveys toward the Galactic Bulge (GB) have been shown to be useful for exoplanet searches, the study of the structure, kinematics and dynamics of the Galaxy, and measurement the stellar and sub-stellar mass functions, as the event rate and timescale distributions are related to the masses and velocities of lens objects (Paczynski 1991, Griest et al. 1991, Novati et al. 2008). To date, several thousands of microlensing events have been detected in the GB by the microlensing survey groups: OGLE (Udalski et al. 1994, 2000; Woźniak et al. 2001; Udalski 2003; Sumi et al. 2006), MOA (Bond et al. 2001; Sumi et al. 2003), MACHO (Alcock et al. 1997, 2000b) and EROS (Afonso et al. 2003; Hamadache et al. 2006). Thousands of detections are expected in the upcoming years from the MOA-II<sup>1</sup>, OGLE-IV<sup>2</sup>, and WISE<sup>3</sup> (Shvartzvald & Maoz 2012) sur-

---

<sup>1</sup><http://www.massey.ac.nz/~iabond/alert/alert.html>

<sup>2</sup><http://www.astrouw.edu.pl/~ogle/ogle4/ews/ews.html>

<sup>3</sup><http://wise-obs.tau.ac.il/~wingspan/>

veys, which are currently in operation. These surveys will soon be joined by the KMTNet survey (Kim et al. 2010).

The magnification of a microlensing event is described by (Paczynski 1986)

$$A(u) = \frac{u^2 + 2}{u\sqrt{u^2 + 4}}, \quad (1)$$

where  $u$  is the projected separation of the source and lens in units of the Einstein radius  $R_E$  which is given by

$$R_E(M, x) = \sqrt{\frac{4GM}{c^2} D_s x (1 - x)}, \quad (2)$$

where  $M$  is the lens mass,  $x = D_l/D_s$  is the normalized lens distance and  $D_l$  and  $D_s$  are the observer-lens and the observer-source distances. The time variation of  $u = u(t)$  is

$$u(t) = \sqrt{u_0^2 + \left(\frac{t - t_0}{t_E}\right)^2}, \quad (3)$$

where  $u_0$ ,  $t_0$ ,  $t_E = R_E/v_t$  and  $v_t$  are, respectively, the minimum impact parameter in units of  $R_E$ , the time of maximum magnification, the Einstein radius crossing time (or timescale), and the transverse velocity of the lens relative to the line of sight toward the source star. From light curve alone, one can determine the values of  $u_0$ ,  $t_0$  and  $t_E$ , but not the values of  $M$ ,  $x$  or  $v_t$ .

The microlensing optical depth,  $\tau$  is the fraction of the sky covered by the Einstein ring disks of the lenses for a given source population, and it is directly related to the mass density of compact objects along the line of sight (Paczynski 1996). Theoretically, it is simpler than the microlensing event rate,  $\Gamma$ , because it doesn't depend on the lens and source velocity distribution. Practically, it is difficult to measure, however, because long duration events give a large contribution to  $\tau$ , and it is difficult to ensure that there is not a significant contribution from events with a duration longer than the maximum  $t_E$  for a given analysis. Because of this, we present observed values of the optical depth with a subscript, which indicates the maximum  $t_E$  value allowed by the analysis of each observational sample.

Despite this ambiguity due to long duration events, previous Galactic bulge microlensing optical depth results have been somewhat controversial. Paczynski (1991) and Griest et al. (1991) first predicted the optical depth of  $\tau \sim 5 \times 10^{-7}$ , assuming that all events were associated with known disk stars. After the first several bulge events were reported by

OGLE (Udalski et al. 1994) and MACHO (Alcock et al. 1995), the high event rate prompted Kiraga & Paczyński (1994) to evaluate the contribution of bulge stars in addition to the disk stars. They estimated  $\tau \sim 8.5 \times 10^{-7}$  and concluded that the value could be about twice as large, if the bulge were elongated along the line of sight. Nevertheless, the first measurements of the optical depth,  $\tau_{100} \sim 3.3 \times 10^{-6}$  by OGLE (Udalski et al. 1994) and  $\tau_{150} \sim 3.9^{+1.8}_{-1.2} \times 10^{-6}$  by MACHO (Alcock et al. 1997), were well above the predictions. The later studies based on Difference Image Analysis (DIA), which is less sensitive to the systematics of blending in crowded fields, also found relatively large optical depths:  $\tau_{150} = 2.43^{+0.39}_{-0.38} \times 10^{-6}$  centered at  $(l, b) = (2.^{\circ}68, -3.^{\circ}35)$  from 99 events by MACHO (Alcock et al. 2000b) and  $\tau_{150} = 2.59^{+0.84}_{-0.64} \times 10^{-6}$  centered at  $(l, b) = (3.^{\circ}0, -3.^{\circ}8)$  from 28 events by MOA (Sumi et al. 2003) (where the dubious adjustment factor to “correct” for foreground disk stars has not been used.) This MACHO DIA analysis had one known  $t_E \sim 500$ -day event that was removed by the  $t_E < 150$  day cut, and the inclusion of this single event would have raised the measured  $\tau$  value by  $\sim 15\%$ .

To explain high optical depths a number of authors have suggested the presence of a bar oriented along our line of sight to the GB (Paczynski et al. 1994; Zhao, Spergel & Rich 1995), and have adopted various values of the bar orientation and mass (Han & Gould 2003; Zhao & Mao 1996; Peale 1998; Gyuk 1999). The resulting values are in the range  $\tau = 0.8 - 2.0 \times 10^{-6}$ . Binney et al. (2000) have shown that high optical depth measurements available at the time could not be easily reconciled with our general understanding of the Galactic dynamics, and that the standard models of the Galaxy would need to be revised.

Alcock et al. (1997) raised the possibility of a systematic bias in the optical depth measurement due to the difficulties of measuring  $t_E$  associated with blended unresolved sources. When the actual source base-line flux is unknown,  $t_E$  and  $u_0$  are degenerate in relatively low signal-to-noise ratio (S/N) events (c.f. Woźniak & Paczyński 1997; Han 1999; Bond et al. 2001; Gould & An 2002). Popowski et al. (2001) postulated that optical depth may be estimated without a bias due to blending by using only events with bright source stars, such as red clump giants, in which they thought that the blending might be negligible, rather than using all stars including the faint sources as in previous studies. Although the first measurements by Alcock et al. (1997) gave a high value  $\tau_{150} \sim 3.9^{+1.8}_{-1.2} \times 10^{-6}$ , the later measurements based on events with bright sources have returned lower optical depths:  $\tau_{400} = 0.94 \pm 0.29 \times 10^{-6}$  at  $(l, b) = (2.^{\circ}5, -4.^{\circ}0)$  from 16 events by EROS (Afonso et al. 2003),  $\tau_{350} = 2.17^{+0.47}_{-0.38} \times 10^{-6}$  at  $(l, b) = (1.^{\circ}50, -2.^{\circ}68)$  from 42 events by MACHO (Popowski et al. 2005), and  $\tau_{400} = (1.62 \pm 0.23) \exp[-a(|b| - 3\text{deg})] \times 10^{-6}$ , with  $a = (0.43 \pm 0.16)\text{deg}^{-1}$  based on 120 EROS events (Hamadache et al. 2006).

All the bright star analyses discussed above have one drawback compared to the DIA

analyses of Alcock et al. (2000b) and Sumi et al. (2003). In each case, the analysis implicitly assumes that the events that occur at the approximate location of a bright star are due to lensing of the bright star and not some much fainter star at almost the same location. Actually, Popowski et al. (2005) and Hamadache et al. (2006) realized that lensing of a fainter star that is unresolved from the bright star would be relatively common. However, they presented arguments that this would increase the apparent number of bright star events, but it would also lead to shorter apparent event durations. They argued that these two effects would nearly cancel, so that these apparently severe blending effects would not lead to a large bias in the optical depth. A comparison with theory seemed to support this conclusion. These values are consistent with predictions based on the revised COBE bar model by Han & Gould (1995), which has a mass of  $M_{\text{bulge}} = 1.62 \times 10^{10} M_{\odot}$  and the viewing angle  $\phi \sim 20^\circ$ , and the latest COBE elongated bar model by Bissantz & Gerhard (2002) with  $\phi \sim 20^\circ$ .

Although the optical depth results from the bright RCG sources and the fainter sources from the DIA analyses are generally consistent within their error bars, the DIA optical depth values are about 25% larger than the RCG values. The reason for this is not well understood. One possibility is that the difference is simply statistical, and it is just a coincidence that the two all-source analyses have given larger optical depths than the RCG analyses. Sumi et al. (2006) and Smith, Woźniak, Mao & Sumi (2002) conducted detailed image level simulations on systematics due to the blending, and found that the bright RCG samples do suffer from systematic errors and suffer biases although the biases do tend to cancel at the level of the statistical uncertainties in previous work, in agreement with Popowski et al. (2005) and Hamadache et al. (2006). Sumi et al. (2006) measured the Galactic bulge optical depth from OGLE-II data for RCG sources with high signal-to-noise light curves, which allowed the source brightness to be determined from the microlensing light curve fit. This allowed the source brightness to be determined so that RCG “impostor” events, with faint sources, could be excluded. This yielded an optical depth value,  $\tau_{150} = 2.55_{-0.46}^{+0.57} \times 10^{-6}$  at  $(l, b) = (1.^\circ 16, -2.75^\circ 8)$ , slightly higher than, but quite consistent with the MACHO and EROS values. This value is also slightly lower than the analyses using DIA photometry of events with fainter sources. This suggests that this difference in the optical depth for the bright and faint star samples might be due to some physical effect, as was seen in the models of Kerins, Robin & Marshal (2009). However, another possibility is that there is a problem with estimating the number of sources as a function of position in the bulge.

While the previous discussion has focused on the microlensing optical depth, due to its simpler theoretical interpretation, the microlensing rate has a number of advantages. It is a more direct measure of the number of microlensing events that will be seen by a future space-based microlensing survey (Bennett & Rhie 2002), like the exoplanet microlensing survey

planned for WFIRST (Green et al. 2012) or Euclid (Penny et al. 2013). The event rate has smaller uncertainties because it is not dominated by a small number of very long duration events.

In this paper we present a measurement of the microlensing event rate and optical depth toward the GB based on the first two years of the MOA-II survey, the second phase of the MOA experiment. Our analysis makes use of only high S/N events with well constrained model parameters to avoid the ambiguities due to parameter degeneracies caused by blending. We present the photometric data in section §2 and the selection of microlensing events in section §3. In section §4, we present the computation of the detection efficiency, and we present the event rate and optical depth results in section §5. In section §6, we discuss models of the variation of the event rate and optical depth with galactic coordinates, and we discuss our results and present our conclusions in section §7,

## 2. Data

The data set used in this analysis is same as used by Sumi et al. (2011). That is, it was taken in the 2006 and 2007 seasons by the MOA-II survey, with the 1.8-m MOA-II telescope located at the Mt. John University Observatory, New Zealand. The telescope is equipped with the wide field camera, MOA-cam3, which consist of ten  $2k \times 4k$  pixel CCDs with  $15 \mu m$  pixels. With the pixel scale of 0.58 arcsec/pixel scale (Sako et al. 2008), this gives a  $2.18 \text{ deg}^2$  field of view (FOV). The median seeing for this data set was  $2.0''$ .

The MOA-II survey is a high cadence photometric survey of millions of stars in 22 GB fields. The centers of these fields are listed in Table 1, although field 22 was not used in this analysis, due to its distance from the bulge. The data consists of  $\sim 8250$  images of each of the two most densely sampled fields, gb5 and gb9, with a 10 minute sampling cadence, and 1660-2980 images of each of the 19 other fields, which were sampled with a 50 minute cadence, as indicated in Table 1. This high cadence strategy is designed to detect very short events with  $t_E < 2$  days, which are expected due to lensing by free-floating planets (Sumi et al. 2011) and short planetary anomalies in the light curves of stellar microlensing events (Mao & Paczyński 1991; Sumi et al. 2010; Bennett 2008; Gaudi 2012). This high cadence also increased the fraction of the events in which the lensing parameters are well constrained by the light curve fit, which is very important for precise measurements of the microlensing rate and optical depth.

The images were reduced with MOA’s implementation (Bond et al. 2001) of the difference image analysis (DIA) method (Tomany & Crotts 1996; Alard & Lupton 1998; Alard

2000). In the DIA method, a high quality, good seeing, reference image is subtracted from each observed image after transforming the reference image to give it the same seeing and photometric scaling as the observed image. This method generally provides more precise photometry in the very crowded Galactic bulge fields than PSF-fitting routines, such as DOPHOT (Schechter, Mateo & Saha 1993). This is, in part, due to the fact that the GB fields are so crowded that virtually all the main sequence stars are not individually resolved. As described in Section 4, the identification of a clear RCG population in the data is needed to match the observed MOA luminosity function to the much deeper Hubble Space Telescope (HST) luminosity function (Holtzman et al. 1998) that describes the source stars. This is similar to the OGLE-II optical depth analysis (Sumi et al. 2006) that makes use of the OGLE-II extinction map (Sumi 2004), which is based on the RCG position in the color magnitude diagram (CMD) of each field.

Each field is divided into 80 subfields and each subfield is individually calibrated using the RCG feature in each subfield CMD. For the gb22 field and some fraction of other fields, totaling about 12% of the area, a clear RCG population could not be identified in the CMD, and these regions were excluded from the analysis for this reason. The number of subfields used in the final analysis is 1536 in total and also given in Table 1 for each field, where the maximum is 79 as one subfield is not useful for a technical reason. The coordinates and other information of subfields are listed in Table 2. This lack of a clear RCG feature in field gb22 is because it is relatively far from the center of the Galaxy. For the other fields, It is generally regions of very high interstellar extinction that prevented the identification of the RCG CMD feature in some of the subfields.

The images were taken using the custom MOA-Red wide-band filter, which is equivalent with the sum of the standard Kron/Cousins  $R$  and  $I$ -bands. The instrumental magnitudes of the MOA reference images were calibrated to the Kron/Cousins  $I$ -band using OGLE-II photometry map of the Galactic bulge (Udalski et al. 2002). The mean magnitude zero-point were estimated from the 30% of MOA-II fields which overlap with the OGLE-II map. We applied this mean zero-point to all fields. The uncertainty in the magnitudes calibrated by this procedure is estimated to be  $\sim 0.25$  mag from the standard deviation of zero-points in overlap fields. Although this calibration is approximate, it does not affect following analysis at all because the luminosity functions, which is the only part of our analysis requiring calibrated magnitudes, are calibrated by using the RCG CMD feature, as discussed in Section 4.

### 3. Microlensing event selection

We make use of the same microlensing events selected in the analysis of Sumi et al. (2011). The processes and criteria for event selection have been developed for that paper and are reused for the current analysis. Event selection details are summarized in Table S2 and Section 2 of the Sumi et al. (2011) Supplementary Information (SI).

In short, we have selected light curves with a single instantaneous brightening episode and a flat constant baseline, which can be well fit with a point-source, point-lens (PSPL) microlensing model given by Eq. (1), with separate parameters for both the source and blend fluxes. We required that the lensing parameters are well constrained by the light curve model, including both the source and blend fluxes, with the minimum impact parameter of  $u_0 < 1.0$ . Binary lens events are excluded from this analysis with a strict cut on the  $\chi^2$  of the PSPL model. Although we have identified more than a thousand microlensing candidates in this data set, only 474 high quality microlensing events have passed our relatively strict cuts on the error bars of the event parameters as determined by the microlensing model fit. These strict criteria ensure that  $t_E$  is well constrained for each event and that there is no significant contamination by mis-classified events. Thus, they ensure that the event rate and optical depth measurements are not significantly biased by low-level systematic errors in the event parameters. The agreement of the observed and simulated  $u_0$  distributions, shown in Fig. S4 in the SI of Sumi et al. (2011) support the conclusion that systematic errors or contamination by non-microlensing variability are negligible. Fig. S5 of the SI indicates that the systematic bias between input and the fit  $t_E$  of simulated events is  $\lesssim 5\%$  level regardless of  $t_E$  as seen in Fig. S5 of SI in Sumi et al. (2011), which also support the negligible bias in our optical depth estimates.

The number of selected events,  $N_{ev}$ , in each field and subfield are listed in Tables 1, 2 and 3, respectively. In Table 4, we list the microlensing events with the best fit parameters, with the complete list available in the online, electronic edition, and a sample available in the print edition.

#### 3.1. Defining Source Populations

For the microlensing rate and optical depth estimates, we use two subsamples of events: (1) the all-sources sample, with events brighter than  $I_s \leq 20$  mag, and (2) the Red Clump Giant (RCG) sample, the stars in the "extended RCG region" as shown in Figure 1, which is a similar definition as previous works. This will allow us to see if there is a discrepancy as was seen in previous studies.



(1) The "all source" sample uses all 474 events mentioned above. In this sample, the events with the best fit source magnitude of fainter than  $I_s = 20$  mag have been rejected to avoid the possible contamination from the events with degenerate parameters.

(2) The RCG sample uses 83 events with source magnitudes of  $I_s < 17.5$  mag and the source colors of  $(V - I)_s \geq (V - I)_{\text{RC}} - 0.3$  mag, where  $(V - I)_{\text{RC}}$  is the  $V - I$  color of RCG centroid. The RCG centroid  $(V - I, I)_{\text{RC}}$  was identified in each subfield by a method very similar to that of Nataf et al. (2012). This RCG sample is similar to the ones in the previous RCG microlensing optical depth paper papers (Alcock et al. 1997; Popowski et al. 2005; Sumi et al. 2006; Hamadache et al. 2006), which contain not only the bulge RCG, but also contain other bulge red giants in the "extended RCG region" of the CMD as shown in Figure 1. Because we don't have  $V$ -band source magnitudes from the light curve models, we use the  $V$  and  $I$  photometry of stars on the reference image at the position of the event for the source color,  $(V - I)_s$ . Our event detection method on the difference images does not require the star to be associated with an apparently resolved reference image star, but we do require that fit source magnitudes are  $I_s < 17.5$  mag. So, in almost all cases, the bright star will be the source or the source blended with another bright star. A fraction of these bright stars and events do not have  $V - I$  photometry, mostly due to high extinction, which renders the stars undetectable in the  $V$ -band. Since a blue star would have to be intrinsically very bright to pass the  $I_s < 17.5$  mag cut in these high extinction regions, these stars are very likely to satisfy our color requirement, even though we are unable to verify that they do. In practice, we have rejected only stars that have a clear measurement of  $V - I$  with  $(V - I)_s < (V - I)_{\text{RC}} - 0.3$ . We have kept the rest of them, because the purpose of color cut is to reduce the contamination from foreground disk stars as much as possible. We have used this condition for both selecting events and counting source stars for our RCG sample.

#### 4. Detection efficiency

We use the detection efficiency determined by Sumi et al. (2011), as described in Sections S4 of the SI of that paper, but we briefly summarize our method here. The detection efficiency of our survey was determined with Monte Carlo simulations following Sumi et al. (2003). Artificial microlensing events were added at random positions to the observed images, using PSFs derived from nearby stars in each field. The parameters of these artificial events were uniformly generated at random in the following ranges for the impact parameter,  $u_0$ , time of peak magnification,  $t_0$ , Einstein radius crossing time,  $t_E$ , and source magnitude,  $I_s$ :  $0 \leq u_0 \leq 1.5$ ,  $2453824 \leq t_0 \leq 2454420$  JD,  $0.1 \leq t_E \leq 250$  days, and  $14.25 \leq I_s \leq 21.0$  mag. (The  $t_0$  range is the range of observations in this data set.) Although we select only

events with  $I_s < 20$  mag, we simulate stars down to  $I = 21$  mag in our detection efficiency calculations to take account the fact that some events with sources magnitudes that are fainter than  $I = 20$  mag can be selected, due to the fit uncertainty in the source magnitude values. We simulated events with up to  $u_0 \leq 1.5$  for the same reason. The source magnitudes were weighted by the combined Luminosity Function (LF) from MOA-II and the *Hubble Space Telescope* (HST) (Holtzman et al. 1998). This uses the MOA-II LF at a subfield of gb13-5-4 for bright stars and HST for faint stars down to  $I = 24$  mag. (Subfield gb13-5-4 is the one that contains the Holtzman et al. (1998) Baade’s WIndow field.) This combined LF is calibrated to the extinction and Galactic bulge distance for each subfield using the position of the RCG centroid in each CMD, because RCG stars serve as a good standard candle (Kiraga, Paczyński & Stanek 1997; Stanek et al. 2000). Subfields where the RCG feature in the CMD could not be clearly identified were not used in this analysis.

Once the images with artificial events were created, they were processed with the same analysis pipeline and selection criteria used for the analysis of the actual data. We evaluated our detection efficiency as a function of  $t_E$ ,  $\varepsilon(t_E)$ , in each field by simulating 20 million artificial events as shown in Figure 2. For Einstein radius crossing times of 1-50 days, the RCG efficiency is higher, as one would expect, but the RCG efficiency drops steeply for events with  $t_E \gtrsim 80$  days. This is an artifact of the original purpose of this analysis, which was to study the short timescale tail of the  $t_E$  distribution in order to search for a population of free-floating planets (Sumi et al. 2011). The original event selection procedure included a cut on the  $\chi^2$  for a constant brightness fit for data outside of a 120-day window centered on the peak of the event. Long duration events with bright sources are much more likely to fail this cut.

In addition to the detection efficiency for each field as a function of the event timescale,  $\varepsilon(t_E)$ , we have also determined the detection efficiency, averaged over  $t_E$ , in each subfield,  $\langle \varepsilon \rangle = \Sigma[f(t_E)\varepsilon(t_E)]/\Sigma f(t_E)$ , where  $f(t_E)$  is the  $t_E$  distribution appropriate for each subfield. Because we do not know the true  $t_E$  distribution for each subfield, we use a Gaussian weighted average of the observed detection efficiency corrected  $t_E$  distribution for all the other subfields within 1 degree the subfield in question. The Gaussian weighting uses  $\sigma = 0^\circ.4$  for the all-star sample, and for the RCG sample, we use  $\sigma = 1^\circ$  degree for all sub-fields out to  $2^\circ.5$  from the subfield in question. The average efficiencies for each subfield are listed in Tables 2 and 3 for the all-star and RCG samples, respectively. These  $\langle \varepsilon \rangle$  will be used for analysis of event rates in the next section. The average timescales for all source with 1 degree radius and  $\sigma = 0.4$  degree are also shown in these tables and in the first panel of Figure 3.

## 5. Microlensing Event Rate and Optical Depth

The microlensing event rate,  $\Gamma$ , can be determined observationally from the following expression,

$$\Gamma = \frac{1}{N_s T_o} \sum_i \frac{1}{\varepsilon(t_{E,i})}, \quad (4)$$

where  $N_s$  is the total number of source stars monitored for microlensing,  $T_o$  is the duration of the survey in days,  $t_{E,i}$  is the Einstein radius crossing time for the  $i$ -th event, and  $\varepsilon(t_{E,i})$  is the detection efficiency at that time-scale. The optical depth,  $\tau$ , is the probability that a random star is microlensed with the impact parameter  $u_0 \leq 1$  at any given time. This is equivalent to the fraction of the total observing time per star that a lens is within the angular Einstein radius of one of the source stars. This depends on the impact parameter,  $u_0$ , but since the distribution in  $u_0$  is uniform, we can use the average event duration (defined as the time when  $u < 1$ ), which is given by  $(\pi/2)t_E$ . We can substitute this average event duration into equation 4 to obtain the following expression for  $\tau$ ,

$$\tau = \frac{\pi}{2N_s T_o} \sum_i \frac{t_{E,i}}{\varepsilon(t_{E,i})}. \quad (5)$$

However, we can't really measure the full microlensing optical depth, unless we are able to include the very longest duration microlensing events, which have durations of  $t_E \sim 500$  days or more (Poindexter et al. 2005), so the measured values of  $\tau$  include a subscript to indicate the maximum duration of the events in the sample.

In our event rate and optical depth analyses for this 2006-2007 data set,  $T_o = 596.0$  days and the number of source stars is (1)  $N_* = 90.4 \times 10^6$  for all star sample and (2)  $N_{*,RC} = 6.49 \times 10^6$  for the RCG sample. These numbers were determined as follows:

(1) For the all star case, we estimated the center of RCG  $I$ -band magnitude,  $I_{RC}$ , and the number of RCG,  $N_{RC}$  by fitting the Luminosity function of the reference images in each subfield with Equation (4) of Nataf et al. (2012). The combined LF, which is based on LF in Baade's window field (gb13-5-4), are scaled and shifted so that its  $I_{RC}$  and  $N_{RC}$  are same as the values in each subfield. Then the number of stars  $N_s$  are counted down to  $I = 20$  mag by this scaled-combined LF and shown in Table 1 and 2. The advantage of this method is that  $N_{RC}$  is less affected by the blending as they are bright and the shape of LF around this range is roughly symmetric. The disadvantage is that it assumed the LF in all fields are same as that of Baade's window (Holtzman et al. 1998).

(2) For the RCG case, we counted the the number of stars in the reference images in the extended RCG region with  $I < 17.5$  mag and  $(V - I) > (V - I)_{RC} - 0.3$  mag,  $N_{s,RC}$ . They are shown in Table 1 and 3. The advantage of this method is that we are not

assuming that the LF in all fields are same as that of Baade’s window. The disadvantage is that, as discussed in Sumi et al. (2006), the number of sources that can be lensed is slightly overestimated due to blending. The blending makes the stars to be looked brighter overall, however more fainter stars are coming into the the magnitude range than brighter stars going out because the LF is the increasing function towards the fainter stars at  $I \sim 17.5$  mag. Smith, Woźniak, Mao & Sumi (2002) estimated  $N_{s,RC}$  is overestimated by  $\sim 10\%$  by image level simulations. We rescaled  $N_{s,RC}$  down by 10%.

Due to our event selection criteria (e.g., small  $\chi^2/\text{d.o.f.}$  for PSPL fit), all events with significant binary lens features were removed from the sample of event used to determine the event rate and optical depth. The fraction of binary lens events among all microlensing events has been estimated at 8% (Jaroszyński 2002), 6% (Alcock et al. 2000a), 3% (Jaroszyński et al. 2004), 6% (Sumi et al. 2006). We use 6% to correct our optical depth measurement for binary lens events excluded from the sample. The event rate can be corrected by the ratio between the number of events with binary lenses and single lenses is  $0.06/(1 - 0.06)$ . Assuming that the lens system consists of two stars having the same typical time scale, the optical depth contribution of a binary lens event is  $2^{1/2}$  times that of a single lens event. It follows that the optical depth values and their errors have to be rescaled by a factor 1.09.

Individual optical depth estimates for all sources in each field are listed in Table 1, and shown in Figure 4. The second panel of Figure 3 shows a smoothed version of the optical depth centered at the location of each subfield. We also estimated the average optical depth in all fields combined, and found  $\tau_{200} = 1.87^{+0.15}_{-0.13} \times 10^{-6}$  with 474 events for all source sample and  $\tau_{200} = 1.58^{+0.27}_{-0.23} \times 10^{-6}$  with 83 events for RCG sample at  $(l, b) = (1.^{\circ}85, -3.^{\circ}69)$ . The effective line of sight was computed by weighting the number of subfields used. The errors were estimated using the bootstrap Monte-Carlo method of Alcock et al. (1997).

### 5.1. Fitting with Poisson Statistics

The event rate,  $\Gamma$ , and optical depth,  $\tau$ , are expected to be continuous functions of  $l$  and  $b$ . Attempts to measure the  $l$  and  $b$  dependence of have generally involved averaging  $\Gamma$  or  $\tau$  into bins and then fitting functions of  $l$  and  $b$  to the binned data (Popowski et al. 2005; Sumi et al. 2006; Hamadache et al. 2006). There are two problems with this procedure, however. First, the binning necessarily smooths out the intrinsic spacial distribution in  $l$  and  $b$ . Second, individual bins often have a small number of events, but they are nevertheless fit using Gaussian statistics, which do not apply. This leads to large fitting errors if there are bins with 0, 1, or 2 events.

In order to avoid these problems, we introduce a method for fitting with Poisson statistics, and this allows us to fit to the raw, subfield data, even though the average number of events per subfield is  $< 1$ . If the event rate predicted by a given model for a subfield at coordinates  $(l, b)$  is denoted by  $\Gamma_{\text{mod}}(l, b)$ , then the number of expected events in that subfield is given by

$$N_{\text{ev,exp}}(l, b) = \Gamma_{\text{mod}}(l, b) N_s(l, b) T_o < \varepsilon(l, b) > , \quad (6)$$

where  $N_s$  is the number of stars in the subfield,  $T_o$  is the survey duration, and  $< \varepsilon(l, b) >$  is the detection efficiency averaged over  $t_E$  for the subfield at coordinates  $(l, b)$ . These are given in Tables 2 and 3, for the all-star and RCG samples, respectively.

The probability of the observed number of events,  $N_{\text{ev}}(l, b)$ , in the subfield at  $(l, b)$  is

$$P[N_{\text{ev}}(l, b)] = \frac{e^{-N_{\text{ev,exp}}(l, b)} N_{\text{ev,exp}}(l, b)^{N_{\text{ev}}(l, b)}}{N_{\text{ev}}(l, b)!} , \quad (7)$$

according to Poisson statistics. We can then define  $\chi^2 = -2 \ln P[N_{\text{ev}}(l, b)]$  for each subfield, which implies that the  $\chi^2$  for the full fit is

$$\chi^2 = -2 \sum_{(l, b)} \ln P[N_{\text{ev}}(l, b)] = -2 \sum_{(l, b)} \ln \left[ \frac{e^{-N_{\text{ev,exp}}(l, b)} N_{\text{ev,exp}}(l, b)^{N_{\text{ev}}(l, b)}}{N_{\text{ev}}(l, b)!} \right] . \quad (8)$$

This gives the  $\chi^2$  value corresponding to the Poisson probability of the observed number of event. This  $\chi^2$  should generally behave like the more usual  $\chi^2$  from Gaussian statistics, but there is one difference. If  $N_{\text{ev,exp}}(l, b) \approx 1$  for a large fraction of the subfields, then we expect the  $\chi^2$  per degree of freedom to be  $\chi^2/\text{d.o.f.} \approx 2$ . For  $N_{\text{ev,exp}}(l, b) = 1$ ,  $\chi^2 = 2$  is the lowest possible value (obtained for  $N_{\text{ev}}(l, b) = 0$ , or 1). Thus,  $\chi^2/\text{d.o.f.} \approx 1$  is impossible when the number of events per subfield is close to 1. We determine the fit parameter uncertainties by evaluating 68% confidence level with the Markov Chain Monte Carlo (MCMC).

In Section 6, we use this Poisson statistics fitting method for modeling the event rate,  $\Gamma$ , but the modeling of the optical depth,  $\tau$ , is more complicated because of the unequal weighting of events in equation 5. Each event is summed with a weight of  $t_{E,i}/\varepsilon(t_{E,i})$ , so the optical depth does not follow Poisson statistics. Therefore, we use the standard binning method to model the optical depth,  $\tau$ , distribution, but we take care to ensure that none of the bins have a small enough number of events to invalidate the use of Gaussian statistics.

## 6. Modeling the Event Rate and Optical Depth Results

Figure 5 shows the optical depth,  $\tau_{200}$ , as a function of  $b$  for both the all-star and RCG samples. We show the results for the central region with  $|l| < 5^\circ$  to improve the overlap with

previous measurements, which are shown in the same figure. The subfield results have been binned in bins of width  $\Delta b = 0.5^\circ$ . The values for all-source and RCG sample are listed in Tables 5 and 6, respectively.

The optical depth clearly increases with decreasing  $|b|$ , and a simple exponential fit gives,  $\tau_{200} = [2.35 \pm 0.18] \times 10^{-6} \exp[(0.51 \pm 0.07)(3 - |b|)]$  for the all-source sample as indicated by the black solid line in Figure 5. This result is slightly smaller than the measurements by MOA-I (Sumi et al. 2003) and MACHO (Alcock et al. 2000b) with all-source samples. It seems more consistent with the RCG measurements by MACHO (Popowski et al. 2005), EROS-2 (Hamadache et al. 2006) and OGLE-II (Sumi et al. 2006) at  $b \sim -3.5^\circ$ , but somewhat higher at the lower latitude. The exponential model seems to represent the data reasonably well in explaining the optical depth measurements with the all-source sample.

An exponential fit for the optical depth toward RCG sources gives  $\tau_{200} = [1.64 \pm 0.27] \times 10^{-6} \exp[(0.47 \pm 0.17)(3 - |b|)]$ , which is indicated by the red solid line in the Figure 5. This result is consistent with previous RCG measurements. The best linear fit to the OGLE-II RCG measurements is indicated by the red dashed line in Figure 5.

The treatment of blending in the MACHO (Popowski et al. 2005) and EROS (Hamadache et al. 2006) analyses is rather crude. These analyses identify microlensing events solely by their proximity to apparent RCG stars identified in the reference images, with no attempt to determine if the source is a RCG star or a fainter main sequence star. These blending effects will shrink apparent  $t_E$  values for all events, while increasing the number of apparent RCG events. Popowski et al. (2005) and (Hamadache et al. 2006) make arguments to suggest that these two effects approximately cancel. It is plausible that this cancelation still work in the accuracy presented in this analysis.

Note that the  $\tau_{200}$  values for the all-source sample at  $-3^\circ \gtrsim b \gtrsim -4^\circ$ , slightly north Baade’s window in field gb13, are consistent with the values for the RCG sample. However  $\tau_{200}$  is significantly higher for the all-source sample than for the RCG sample at  $b > -3^\circ$ .

Our new optical depth values for the RCG sample are consistent with the previous RCG measurements (Popowski et al. 2005; Sumi et al. 2006; Hamadache et al. 2006) and some older bulge models (Bissantz & Gerhard 2002; Han & Gould 2003) and do agree with the more recent model of Kerins, Robin & Marshal (2009)

The uncertainty in  $\tau$  is dominated by small number of long  $t_E$  events. For this particular analysis, this effect is exacerbated by the low efficiency for events with  $t_E > 100$  days, due to the fact that the analysis was originally designed to focus on short timescale events. The high weight for these long timescale events also means that the error bars for  $\tau$  are difficult to measure. Also, we directly measure  $\tau_{200}$  instead of  $\tau$ , so a comparison to Galactic models

requires a correction based on the rate of very long events, which we don’t measure.

The event rate,  $\Gamma$ , does not have these problems, and so it is the preferred quantity to compare to Galactic models, despite the simple theoretical interpretation of the optical depth,  $\tau$ . We show the event rate per star per year  $\Gamma$  and the exponential fits for the all-source and RCG samples as a function of the galactic latitude,  $b$ , for  $|l| < 5^\circ$  in Figure 6 and in Tables 5 and 6, respectively. The event rate has much less scatter than  $\tau_{200}$  and  $\Gamma$  for both the all-source and RCG samples are well fit by a simple exponential model. Note that these fits are done to the subfield data using our Poisson statistics method (see Section 5.1), while the plots are binned for display in Figure 6 and in Tables 5 and 6.

The exponential model for the all-source and RCG samples are quite similar with  $\Gamma_{\text{all}} = [23.92 \pm 1.13] \times 10^{-6} \exp[(0.60 \pm 0.05)(3 - |b|)]\text{yr}^{-1}$  per star for the all-source sample and  $\Gamma_{\text{RC}} = [21.86 \pm 2.67] \times 10^{-6} \exp[(0.65 \pm 0.11)(3 - |b|)]\text{yr}^{-1}$  per star for the RCG sample. The RCG event rate is slightly smaller, but consistent with the all-source event rate. The RCG slope is  $0.4\sigma$  steeper and the amplitude is  $8\%$  or  $0.7\sigma$  smaller. If we use the all-source model parameters for the RCG sample,  $\chi^2$  increases by only  $\Delta\chi^2 = 0.33$ .

There may be some uncertainty in the true value of  $\Gamma_{\text{all}}$ , due to the uncertainty in the luminosity function. We use the *HST* luminosity function measured in Baade’s window Holtzman et al. (1998), but the true luminosity function could have some dependence on Galactic coordinates. Fortunately, this uncertainty is largely removed for microlensing survey simulations if the same Holtzman et al. (1998) luminosity function is used to estimate the source star counts, as the uncertainty in the luminosity function would largely cancel out.

The need to assume an luminosity function can be avoided entirely by considering the event rate per square degree per year,  $\Gamma_{\text{deg}^2}$ , for source stars above a given magnitude threshold, which is  $I_s \leq 20$  in our case. This quantity is, therefore, more directly determined by the observations. However, unlike  $\Gamma$  and  $\tau_{200}$ ,  $\Gamma_{\text{deg}^2}$  does not depend solely on the distribution of stars and lens objects in the Galaxy. (The lens objects consist of stars, brown dwarfs, planets and stellar remnants.) The event rate per square degree per year,  $\Gamma_{\text{deg}^2}$ , also depends on the foreground extinction. In the Galactic plane,  $\Gamma$  should be maximized but  $\Gamma_{\text{deg}^2}$  could drop to zero if the extinction is so high that no stars are brighter than the magnitude threshold. Figure 7 which shows  $\Gamma_{\text{deg}^2}$  as a function of  $b$  and an exponential fit to the data. The effect of extinction can be seen in the lowest  $|b|$  bin, where  $\Gamma_{\text{deg}^2}$  drops to well below the fit. As with the  $\Gamma$  fits, the fitting was done to the raw subfield data, and the data is binned for display only. The binned  $\Gamma_{\text{deg}^2}$  values are also given in Table 5.

We show exponential fits as a function of the galactic latitude  $b$  for  $\tau_{200}$ ,  $\Gamma$  and  $\Gamma_{\text{deg}^2}$  for different bins in Galactic longitude,  $l$  in Figures 8, 9 and 10, respectively. The black plots

and curves are for all the events with  $-2^\circ.25 < l < 3^\circ.75$ , and it provides a reasonable fit to all the longitude bins, except the  $0^\circ.75 < l < 2^\circ.25$  bin, where there is an enhancement to the rate.

In the second through fourth panels of Figure 3, we display smoothed maps of  $\tau_{200}$ ,  $\Gamma$ , and  $\Gamma_{\text{deg}^2}$  as a function of Galactic coordinates. The plotted values from all subfields are listed in Table 7 of the online version, with a sample of this table listed in the printed version of this paper. The smoothing is done with a Gaussian function with  $\sigma = 0.4^\circ$ , and cut off at a distance of  $1^\circ$  from the center of each subfield. The error bars for each subfield are estimated using a bootstrap method using the neighboring subfields with the same weighting as in the calculation of the central values. As previously found by Alcock et al. (1997) and (Popowski et al. 2005), the highest optical depth is found at  $l \approx 3^\circ$ . This is due to the excess of long timescale events at this longitude, as indicted in the first panel of Figure 3. The longitude of this optical depth maximum is at the same longitude as MACHO field 104, which was noted to have a excess of long timescale events by Alcock et al. (1997) and (Popowski et al. 2005), but we see  $\tau_{200}$  maxima at  $b \approx -2^\circ$  and  $b \approx -5^\circ.5$ , whereas MACHO field 104 is centered at  $b = -3^\circ.1$ . However, this can probably be explained if there is a real excess of long duration events at  $l \approx 3^\circ$  at a range of latitudes. The differences between the MACHO and MOA results can probably be explained by statistical fluctuations and uneven sampling of the  $l \approx 3^\circ$  fields by MACHO.

Both the event rate per star,  $\Gamma$ , and per square degree,  $\Gamma_{\text{deg}^2}$ , have a peak at  $l \approx 1^\circ$ . Because these event rate measurements obey Poisson statistics, the statistical uncertainty in  $\Gamma$  and  $\Gamma_{\text{deg}^2}$  is smaller than the uncertainty in  $\tau_{200}$ . So, we expect that this  $l \approx 1^\circ$  enhancement in the microlensing rate is real and that it is related to the structure and kinematics of the bulge.

Because of the relatively low noise in the  $\Gamma$  and  $\Gamma_{\text{deg}^2}$  measurements, we have fit them with a 16-parameter model in  $l$  and  $b$ . The 16 parameters consist of a 10-parameter cubic polynomial and the inverse of a 6-parameter quadratic polynomial. That is

$$\begin{aligned} \Gamma = & a_0 + a_1 l + a_2 b + a_3 l^2 + a_4 l b + a_5 b^2 + a_6 l^3 + a_7 l^2 b + a_8 l b^2 + a_9 b^3 \\ & + 1/(a_{10} + a_{11} l + a_{12} b + a_{13} l^2 + a_{14} l b + a_{15} b^2) . \end{aligned} \quad (9)$$

The best fit models for  $\Gamma$  and  $\Gamma_{\text{deg}^2}$  are shown in Figure 11 and 12 and the model parameters are listed in Table 8. Both models show the maximum at  $l \approx 1^\circ$  that was also evident in Figure 3.



## 7. Discussion and conclusions

We have measured the microlensing event rate and optical depth toward the Galactic bulge from the first two years of the MOA-II survey. Our sample of 474 events, with well measured parameters is larger than all of the previous samples combined, and we employ a more careful treatment of blending than all previous RCG samples. For the first time, we analyze the event rate and optical depth from for a sample of faint (often unresolved) stars and a RCG sample of 83 events from the same data set. We are able to shed some light on the previously noted difference between the optical depth measured with RCG samples (Popowski et al. 2005; Sumi et al. 2006; Hamadache et al. 2006) and samples of faint stars from DIA photometry surveys (Alcock et al. 2000b; Sumi et al. 2003). The faint star analyses have shown systematically larger  $\tau$  values.

Some of the previous RCG analyses (Popowski et al. 2005; Hamadache et al. 2006) have implicitly assumed that all events occurring in the proximity of RCG stars actually had RCG sources, and then argued that blending caused relatively large errors of both signs, which happened to nearly cancel in the measurement of  $\tau$ . The OGLE-II analysis (Sumi et al. 2006) allowed for blending in the microlensing light curve fits and was, like this analysis, restricted to events with relatively small light curve parameter uncertainties. This allowed events to be selected based on the best fit source brightness, which removes most systematic errors due to blending. However, the photometry used by (Sumi et al. 2006) implicitly assumed that there was no blending, as it was done at the location of the apparent star in the reference frame. In this analysis, we have performed the photometry at the locations of the events as identified in difference images. As a result, we avoid a systematic photometry error for blended events that might affect the Sumi et al. (2006) analysis, and our analysis method should be considered to be an improvement over the methods used for previous RCG optical depth measurements.

Our new all-source optical depth measurements are consistent with all previous measurements for both all-source and RCG samples, with the exception of the EROS (Hamadache et al. 2006), which is more than  $2\text{-}\sigma$  smaller. Our RCG optical depth results are consistent with EROS and the other previous RCG measurements, but we believe that our RCG optical depth may be biased low, due to the low efficiency for long duration RCG events. We can use the exponential models shown in Figure 5 to interpolate our measurement to the center of previous samples. For the MACHO DIA all-source result at  $b = -3^\circ.35$  (Alcock et al. 2000b), we find  $\tau = [1.97 \pm 0.15] \times 10^{-6}$  which is  $1.1\text{-}\sigma$  smaller than the MACHO result of  $\tau = 2.43^{+0.39}_{-0.38} \times 10^{-6}$ , using the combined error bar. The MOA-I all-source result (Sumi et al. 2003), centered at  $b = -3^\circ.8$ , is  $\tau = 2.59^{+0.84}_{-0.64} \times 10^{-6}$ . This compares to our interpolated value of  $\tau = [1.57 \pm 0.12] \times 10^{-6}$ , which is  $1.4\text{-}\sigma$  smaller. Thus, our new optical depth

measurement is smaller at the  $\sim 1\text{-}\sigma$  level than both the previous all-source measurements, which suggests that some of the previously seen difference between the all-source and RCG samples is due to statistical fluctuations.

The only previous RCG sample that distinguished RCG source events from events with main sequence sources that happened to be blended with RCG stars was the OGLE-II analysis of Sumi et al. (2006), and they found  $\tau = 2.55^{+0.57}_{-0.46} \times 10^{-6}$  at  $b = -2^\circ.75$ . This compares to our all-source result, interpolated from the model given in Figure 5, is  $\tau = [2.67 \pm 0.20] \times 10^{-6}$ , which is just  $0.2\text{-}\sigma$  larger. Our RCG result, interpolated from the RCG model in the same figure is  $\tau = [1.84 \pm 0.30] \times 10^{-6}$ , which is just  $1.1\text{-}\sigma$  smaller. The MACHO Collaboration published several averages of their results (Popowski et al. 2005), but we compare to their “CGR+3” average of  $6 \text{ deg}^2$  centered at  $b = -2^\circ.73$ . MACHO reports  $\tau = 2.37^{+0.47}_{-0.39} \times 10^{-6}$  for RCG sources at this position. This compares to our interpolated all-source value of  $\tau = [2.70 \pm 0.21] \times 10^{-6}$ , which is just  $0.7\text{-}\sigma$  larger. Our interpolated RCG value at this position is of  $\tau = [1.86 \pm 0.31] \times 10^{-6}$ , which is  $1.0\text{-}\sigma$  smaller.

The RCG sample of the EROS Collaboration (Hamadache et al. 2006) covers a wider area than the other previous optical depth measurement samples, and in fact, it covers a slightly larger area than the MOA-II analysis that we present here. Fortunately, they fit their results to an exponential model that is identical to the one shown in Figure 5, and they find  $\tau = [1.62 \pm 0.23] \times 10^{-6} \exp[(0.43 \pm 0.16)(3 - |b|)]$ . This has a slope that is consistent with our fits, which are shown in Figure 5, so we can compare our result to theirs by simply comparing the normalization parameter of our models to theirs. For the all-source sample, our normalization parameter is  $[2.35 \pm 0.18] \times 10^{-6}$ , which is  $2.4\text{-}\sigma$  larger than the EROS value of  $[1.62 \pm 0.23] \times 10^{-6}$ . A somewhat more fair comparison would be to compare to the the EROS fit to a model fit to all our fields, instead of just those with  $|l| < 5^\circ$ . This gives  $\tau_{200} = [2.22 \pm 0.16] \times 10^{-6} \exp[(0.52 \pm 0.07)(3 - |b|)]$ , with is  $2.1\text{-}\sigma$  larger than the EROS value. However, our RCG value of  $[1.64 \pm 0.27] \times 10^{-6}$  matches their parameter,  $[1.62 \pm 0.23] \times 10^{-6}$ , to better than  $0.1\text{-}\sigma$ .

In summary, we find that our all-source results are about  $1\text{-}\sigma$  smaller than the previous all-source measurements, and they are within  $1\text{-}\sigma$  of the RCG optical depth values from OGLE and MACHO. The only apparent discrepancy is with the EROS measurement, which is just over  $2\text{-}\sigma$  smaller than our all-source optical depth. Partly, this is because the EROS RCG sample is larger than the OGLE and MACHO ones, so the error bars are smaller. It may also be that the different spatial coverage of the EROS and MOA-II surveys plays a role in this difference. In any case, the odds of one  $2\text{-}\sigma$  outlier out of 5 comparisons are about 25%, so it is fair to say that our all-source optical depth results are consistent with the results for previous all-source and RCG samples.

In any case, we find that our all-source optical depth measurement splits the range of previous measurements, coming in  $\sim 1\text{-}\sigma$  below the previous all-source measurements and matching the MACHO and OGLE RCG measurements to better than  $1\text{-}\sigma$  we find agreement within  $1\text{-}\sigma$  for 2 out of 5 comparisons and within  $2\text{-}\sigma$  for all 5. So, our results are in good agreement with previous measurements. Our RCG optical depth values also match the previous RCG measurements, but as we have explain below, we believe that our RCG results are biased by poor sensitivity to long timescale events.

Our optical depth results agree with many of the models that have been published. Both the Han & Gould (2003) and Wood & Mao (2005) models agree with our all-source optical depth to better than  $1.3\text{-}\sigma$  at  $b = -3^\circ.9$  and  $b = -3^\circ$ , respectively, but the Wood & Mao (2005) model predicts an optical depth lower than the observed value by  $2.8\text{-}\sigma$  or 23% at  $b = -2^\circ$ . Evans & Belokurov (2002) present a number of models, and their “Dwek plus spiral structure” model agrees with our all-source optical depth to  $0.3\text{-}\sigma$ , while their other models predict both higher and lower optical depths. The model of Bissantz & Gerhard (2002) predicted a lower optical depth than previous measurements.

The theoretical modeling paper that comes closest to explaining our results is Kerins, Robin & Marshall (2009). They consider several different event selection cuts: events with a baseline magnitude  $I < 19$ , events with a peak magnitude  $I < 19$ , and events with “standard candle” sources, which are meant to correspond to the RCG measurements. By comparing the contour levels of their optical depth maps, we find that their baseline magnitude  $I < 19$  results seem to match our measurements well. Their  $\tau = 4 \times 10^{-6}$  contour is at  $b = -1^\circ.9$ , where the fit to our measurements predicts  $\tau = [4.12 \pm 0.35] \times 10^{-6}$ , and their  $\tau = 2 \times 10^{-6}$  contour at  $b = -3^\circ.5$ , where the fit to our measurements gives  $\tau = [1.82 \pm 0.15] \times 10^{-6}$ . Our RCG sample gives  $\tau$  values that are 30-40% below their predictions, but as we explain below, this is likely to be due to the dearth of long timescale events in out RCG sample.

Unfortunately, there are no theoretical predictions for the event rates per star,  $\Gamma$ , and per square degree,  $\Gamma_{\text{deg}^2}$ . As discussed above Section 6 and shown in Figures 3, 6, and 7,  $\Gamma$  and  $\Gamma_{\text{deg}^2}$  can be measured more precisely than  $\tau$ . Furthermore,  $\tau$  has an additional systematic uncertainty due to potential very long time scale events, which may contribute significantly to  $\tau$  but not to  $\Gamma$  and  $\Gamma_{\text{deg}^2}$ .

Figure 6 also indicates that the all-source and RCG  $\Gamma$  values differ by only  $\sim 9\%$ , which is much closer than the  $\tau$  values at low latitudes. While the all-source measurements should generally be more robust than the RCG measurements, there is one weak point in all-source analysis. We don’t directly measure the number of sources. Instead we extrapolate to faint magnitudes using the luminosity function of Holtzman et al. (1998). It is reasonable to expect that the ratio of RCG stars to fainter main sequence stars could vary from

the Holtzman et al. (1998) value by 10-20% at low latitudes, where most of the microlensing events are found. If there are more faint stars than predicted by the Holtzman et al. (1998) luminosity function, there would be more microlensing events and a larger  $\Gamma$  would be inferred.

Another significant difference between the all-source and RCG samples is their (efficiency corrected)  $t_E$  distributions, which are shown in Figure 13. The mean timescale of the all-source sample is larger than the mean timescale of the RCG sample. Since  $\tau_{200} \propto \langle t_E \rangle$ , this is the reason why the all-source  $\tau_{200}$  value is larger than the RCG  $\tau_{200}$  value, while the  $\Gamma$  values are consistent with each other. This may be largely due to the low detection efficiency at  $t_E > 100$  days for the bright sources in the RCG sample, which is caused by our requirement that the light curve be well fit by a constant brightness model outside of a 120-day window centered on the event peak. Long duration events with bright sources will deviate significantly from a constant baseline brightness at relatively low magnification, but fainter sources can pass this cut because their photometric error bars are larger. For the all-source sample, events with  $t_E > 80$  days contribute 21% to the measurement of  $\tau_{200}$ , but the RCG sample has no events with  $t_E > 80$  days. This is illustrated in Figure 14, which shows the  $t_E$ -weighted, efficiency corrected, timescale distributions for both the all-source and RCG samples. This is proportional to the contribution to  $\tau_{200}$  for each  $t_E$  bin, and it is clear that the handful of events with  $t_E > 80$  days contribute significantly to  $\tau_{200}$ . This issue will be addressed in a future analysis with a much longer time baseline. It is also possible that the low latitude fields have an excess of faint stars due to contamination from stars on the far side of the Galactic disk, that might also contribute the larger  $t_E$  and  $\tau_{200}$  values for the all-source sample.

It is our goal to measure  $\Gamma$  and  $\tau$  in various directions around the galactic bulge to constrain the model parameters of the barred Galactic bulge. Currently MOA-II detects about 700 event per year and OGLE-IV finds about 1700 events a year. In the near future, we plan to expand this analysis to include thousands of events which have been observed since the end of the 2007 observing season, which is the last season included in this paper.

Another goal of this work is to predict the event rate in the inner Galactic bulge for the future infrared space microlensing survey of the Wide Field Infrared Space Telescope (WFIRST) (Green et al. 2012), which was the top ranked large space mission in the New Worlds, New Horizons (NWNH) 2010 decadal survey. The exoplanet microlensing survey is one of the four major science programs called out in NWNH, and one of two programs designated to drive the mission design, along with the dark energy program. Our results can also be useful to the space exoplanet microlensing survey by Euclid (Penny et al. 2013). The expected microlensing event rate for the WFIRST mission is uncertain because the re-

gion with the highest event rate at the low galactic latitudes, where observations have been sparse. This is partly due to the relatively small area of sky covered by some of the previous microlensing surveys (Sumi et al. 2006), but also because some of the previous surveys were designed for LMC observations and did not use a very red passband (Alcock et al. 2000b; Popowski et al. 2005; Hamadache et al. 2006). The MOA-II survey improves this situation somewhat due to its very wide field and custom red passband that covers combined wavelength range of both the Cousins  $R$  and  $I$ -bands, but an infrared microlensing survey would be preferable. Nevertheless, the measurements we present in this paper do provide the best estimate of the event rate in the inner Galactic bulge to date. For  $3.2 \text{ deg}^2$  of the MOA-II survey area inside  $|b| \leq 3^\circ.0$  and  $0^\circ.0 \leq l \leq 2^\circ.0$ , centered at  $(l, b) = (0^\circ.97, -2^\circ.26)$ , we find  $\Gamma = 4.57^{+0.51}_{-0.46} \times 10^{-5} \text{ yr}^{-1}$  for sources with  $I < 20$ . This is a factor of 1.3 larger than the rate model used for the report of the WFIRST Science Definition Team (SDT) (Green et al. 2012) evaluated at this position. However, the WFIRST SDT used a different model to extrapolate to the lower latitude fields,  $|b| \sim -1^\circ.4$ , that WFIRST will observe. So, the model with  $-2^\circ.25 < l < 3^\circ.75$  presented in Figure 9 predicts a 60% higher event rate than assumed in the report of the WFIRST SDT (Green et al. 2012).

We are grateful to B.S. Gaudi and M. Penny for helpful comments. This MOA project is supported by the grant JSPS18253002 and JSPS20340052. TS acknowledges the financial support from the JSPS, JSPS23340044, JSPS24253004. DPB acknowledges support from NSF grants AST-1009621 and AST-1211875, as well as NASA grants NNX12AF54G and NNX13AF64G.

## REFERENCES

- Afonso, C. et al. 2003, A&A, 404, 145
- Alard C., 2000, A&AS, 144, 363
- Alard C., Lupton R. H., 1998, ApJ, 503, 325
- Alcock, C. et al. 1995, ApJ, 445, 133
- Alcock, C. et al. 1997, ApJ, 486, 697
- Alcock C. et al., 2000a, ApJ, 541, 270
- Alcock C. et al., 2000b, ApJ, 541, 734

- Bennett, D.P, 2008, in *Exoplanets*, Edited by John Mason. Berlin: Springer. ISBN: 978-3-540-74007-0, (arXiv:0902.1761)
- Bennett, D.P. & Rhie, S.H. 2002, *ApJ*, 574, 985
- Binney, J. et al. 2000, *ApJ*, 537, L99
- Binney, J. Gerhard, O. & Spergel, D. 1997, *MNRAS*, 288, 365
- Bissantz, N. & Gerhard, O. 2002, *MNRAS*, 330, 591
- Bond I. A. et al., 2001, *MNRAS*, 327, 868
- Evans N.W., & Belokurov, 2002, *ApJ*, 567, 119
- Dwek, E. et al. 1995, *ApJ*, 445, 716
- Gaudi, B. S. 2012, *ARA&A*, 50, 411
- Gould, A. & An, J. H. 2002, *ApJ*, 565, 1381
- Green, J. et al., 2012, preprint, astro-ph/1208.4012
- Griest, K., et al. 1991, *ApJ*, 372, L79
- Gyuk, G. 1999, *ApJ*, 510, 205
- Hamadache, C., Le Guillou, L., Tisserand, P., et al. 2006, *A&A*, 454, 185
- Han, C. & Gould, A. 1995, *ApJ*, 449, 521
- Han, C. & Gould, A. 2002, *ApJ*, 592, 172
- Han, C. 1999, *MNRAS*, 309, 373
- Holtzman, J. A., Watson, A. M., Baum, W. A., et al. 1998, *AJ*, 115, 1946
- Jarosziński, M., 2002, *Acta Astronomica*, 52, 39
- Jaroszyński, M. et al., 2004, preprint, astro-ph/0408243
- Kerins, E., Robin, A. C., & Marshal, D. J. 2009, *MNRAS*, 396, 1202
- Kim, S.-L., Park, B.-G., Lee, C.-U., et al. 2010, *Proc. SPIE*, 7733, 77733
- Kiraga, M., & Paczyński, B. 1994, *ApJ*, 430, L101

- Kiraga, M., Paczyński, B. & Stanek, K. Z., 1997, *ApJ*, 485, 611
- Mao, S., & Paczyński, B. 1991, *ApJ*, 374, L37
- Moniez, M. 2010, *General Relativity and Gravitation*, 42, 2047
- Nataf, D. M., et al. 2012, *arXiv1208.1263*
- Novati S.C., Luca, F. De., Jetzer, Ph., Mancini, L., & Scarpetta, G. 2008, *A&A*, 480, 723
- Paczynski, B. 1986, *ApJ*, 304, 1
- Paczynski, B. 1991, *ApJ*, 371, L63
- Paczynski, B. et al. 1994, *ApJ.*, 435, L113
- Paczynski, B. 1996, *ARA&A*, 34, 419
- Peale, S. J. 1998, *ApJ*, 509, 177
- Penny, M. T., Kerins, E., Rattenbury, N., et al. 2013, *MNRAS*, submitted (*arXiv:1206.5296*)
- Poindexter, S., et al. 2005, *ApJ*, 633, 914
- Popowski, P. et al. 2001, in *ASP Conference Series: Microlensing 2000: A New Era of Microlensing Astrophysics*, eds. J.W. Menzies & P.D. Sackett (San Francisco: Astronomical Society of the Pacific), Vol. 239, p. 244, (*astro-ph/0005466*)
- Popowski, P. et al., *ApJ*, 631, 879
- Sako, T., et al. 2008, *Experimental Astronomy*, 22, 51
- Schechter, L., Mateo, M., & Saha, A., 1993, *PASP*, 105, 1342S
- Shvartzvald, Y., & Maoz, D. 2012, *MNRAS*, 419, 3631
- Smith, M. C., Woźniak, P. R., Mao, S. & Sumi, T., 2007, *MNRAS*, 380, 805
- Stanek, K. Z. et al. 2000, *Acta Astronomica*, 50, 191
- Sumi, T., 2004, *MNRAS*, 349, 193
- Sumi, T. et al., 2003, *ApJ*, 591, 204
- Sumi, T. et al., 2006, *ApJ*, 636, 240
- Sumi, T. et al., 2010, *ApJ*, 710, 1641

- Sumi, T. et al., 2011, *Nature*, 473, 349
- Tomany, A. B. & Crotts, A. P., 1996, *AJ*, 112, 2872
- Udalski A., Zebbruń K., Szymański, M., Kubiak M., Pietrzyński G., Soszyński I., Woźniak P. R. 2000, *Acta Astronomica*, 50, 1
- Udalski, A. et al. 1994, *Acta Astronomica*, 44, 165
- Udalski A. et al. 2002, *Acta Astronomica*, 52, 217
- Udalski, A. 2003, *Acta Astronomica*, 53, 291
- Wood, A., & Mao, S. 2005, *MNRAS*, 362, 945
- Woźniak P. R., & Paczyński, B. 1997, *ApJ*, 487, 55
- Woźniak, P. R., et al. 2001, *Acta Astronomica*, 51, 175
- Zhao, H. & Mao, S. 1996, *MNRAS*, 283, 1197
- Zhao, H., Spergel, D. N. & Rich, R. 1995, *ApJ*, 440, L13



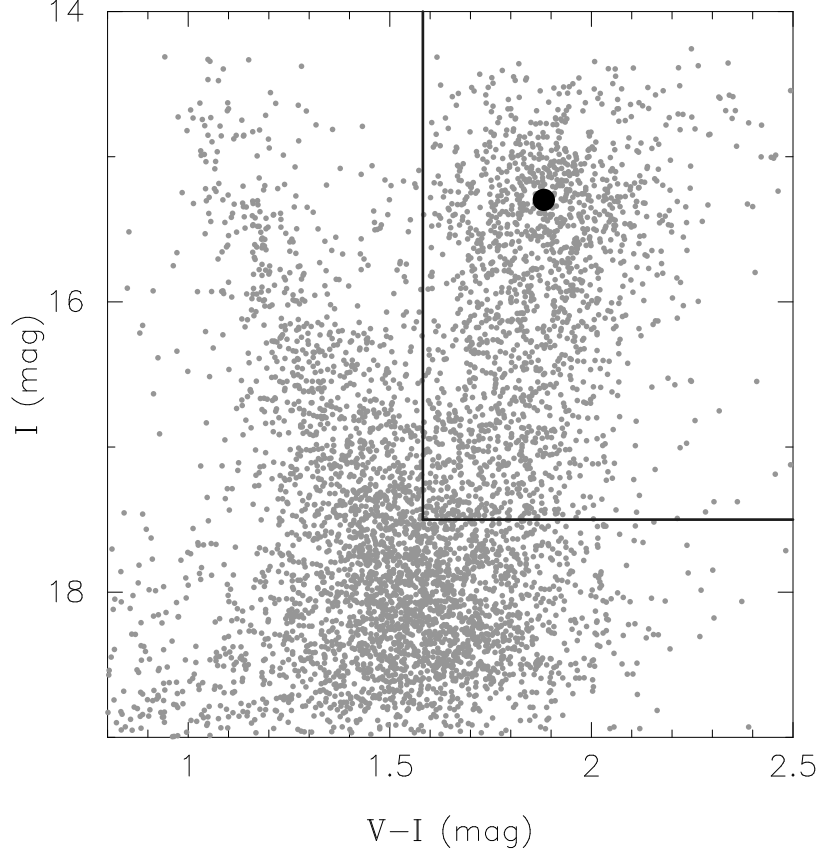


Fig. 1.—: The  $(V - I, I)$  color magnitude diagram of a subfield, gb13-8-3 at  $(l, b) = (2.^\circ 10, -4.^\circ 05)$ . The filled circle indicates the RCG centroid,  $(V - I, I)_{\text{RC}}$ . The stars in "extended RCG region" defined by the solid lines, i.e.,  $I < 17.5$  mag,  $V - I \geq (V - I)_{\text{RC}} + 0.3$  mag are used for our RCG sample.

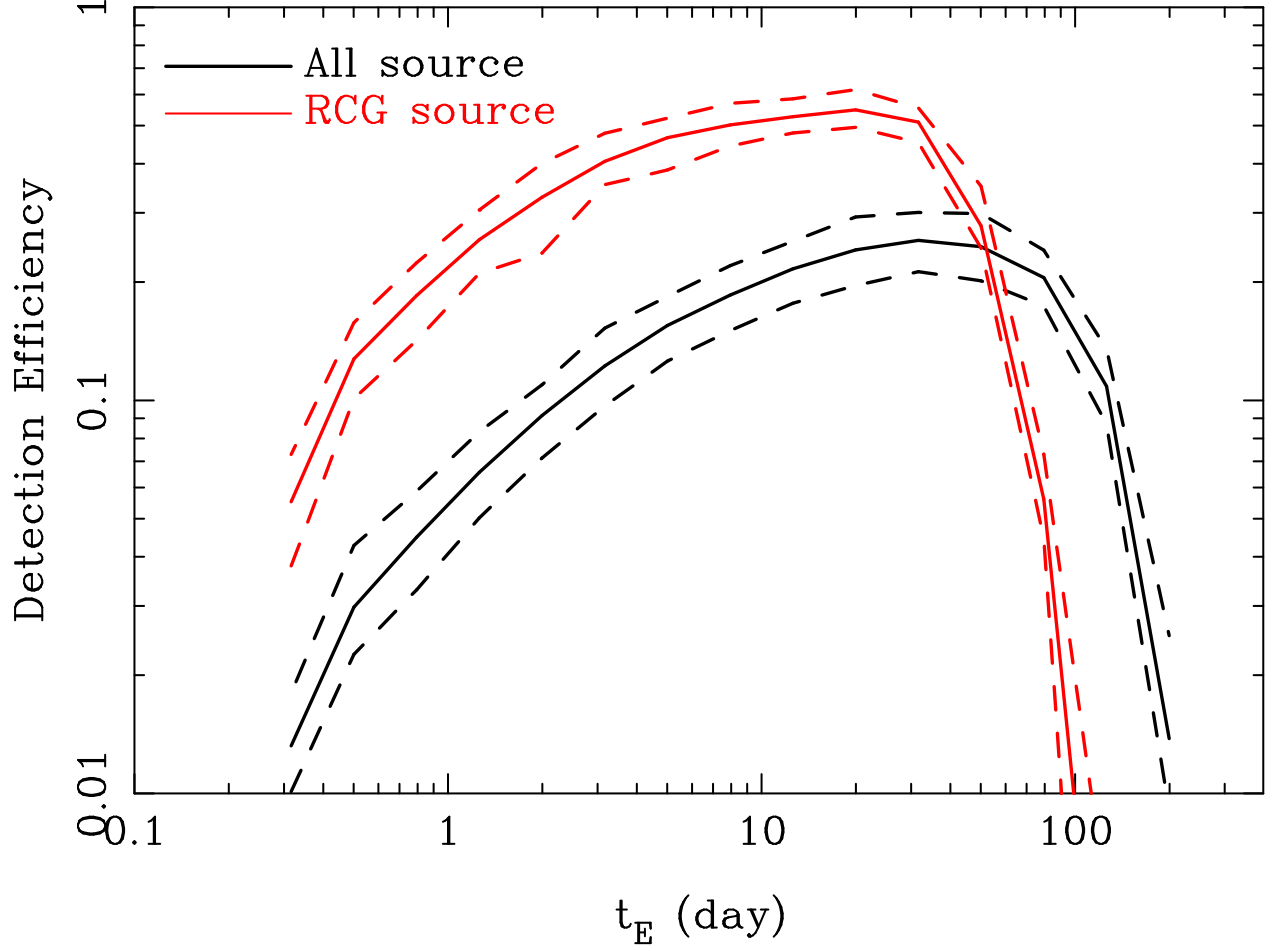


Fig. 2.— The detection efficiencies of the MOA-II survey as a function of  $t_E$  for the all-source sample in black and RCG sample in red. Solid and dashed lines indicate the mean, minimum and maximum efficiencies of all fields, respectively.

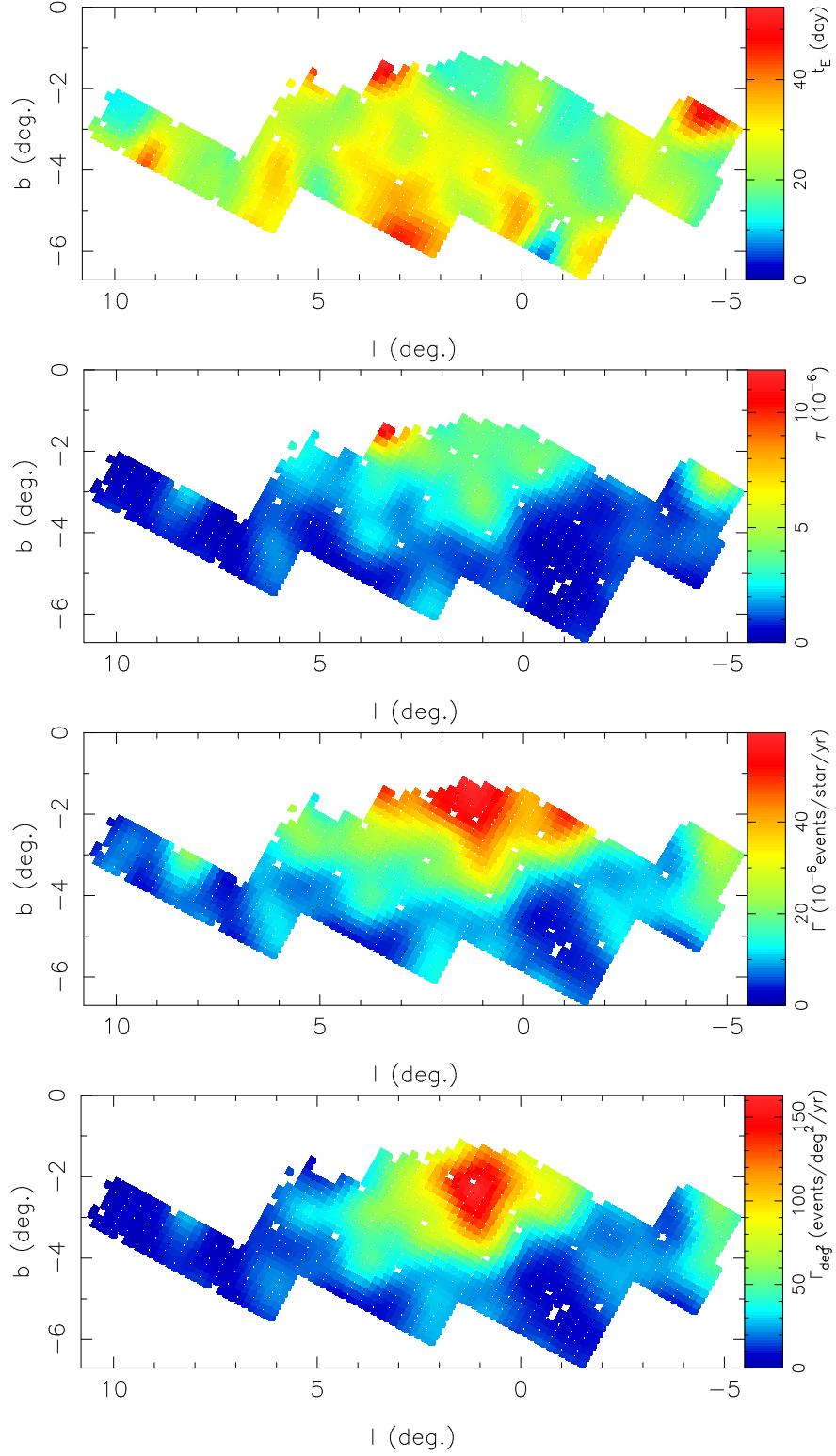


Fig. 3.—: False color maps of the mean event timescale,  $\langle t_E \rangle$ , the measured optical depth,  $\tau_{200}$ , the event rate per star per year,  $\Gamma$ , and the event rate per square degree per year,  $\Gamma_{\text{deg}^2}$ , from top to bottom.

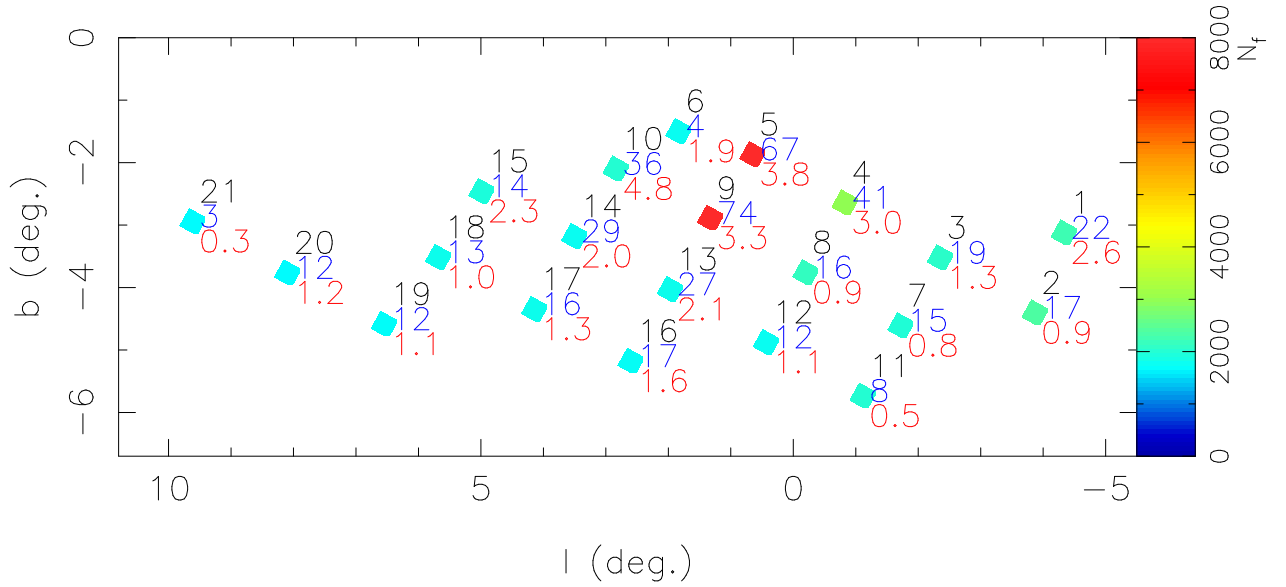


Fig. 4.—: MOA-II galactic bulge fields used in this analysis. The central galactic coordinates of fields are indicated by diamonds with field numbers (in black), the number of events (blue) and the optical depth  $\tau_{200} \times 10^6$  (red) for the all-source sample. The color of the diamonds indicates the number of images per field,  $N_f$ , as indicated by the color scale on the right.

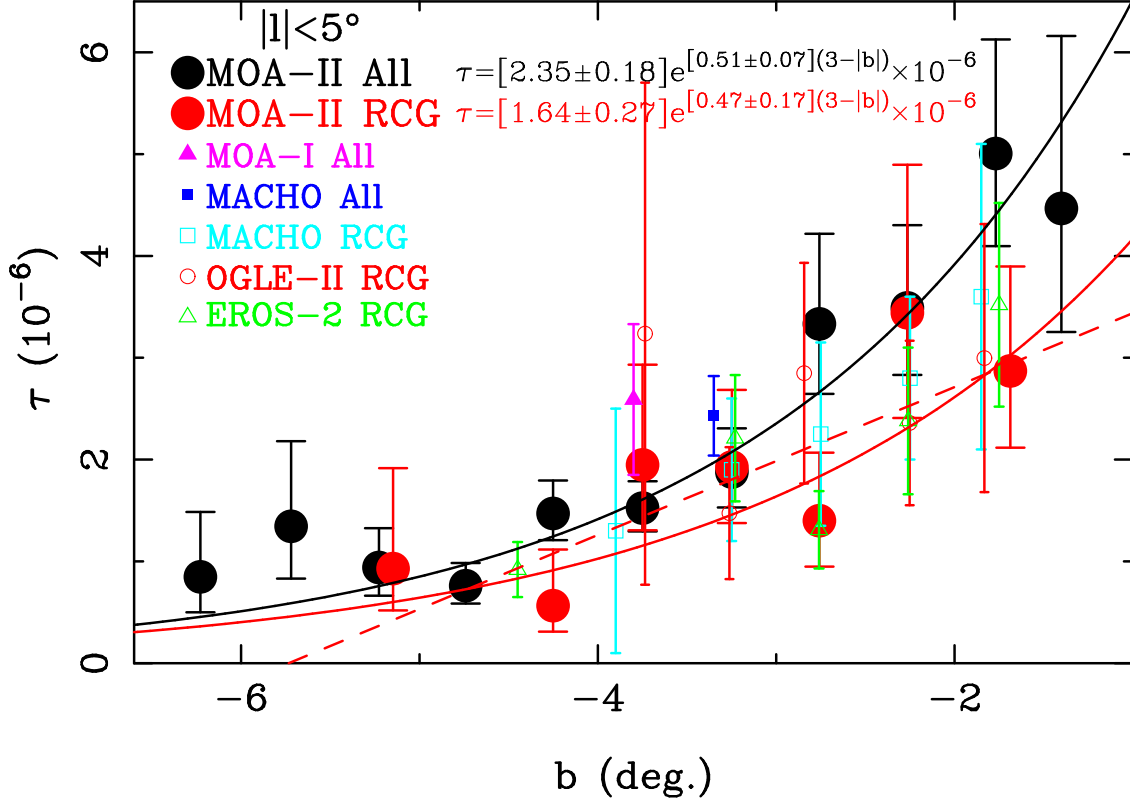


Fig. 5.—: The measured optical depth for the all-source (black filled circle) and RCG (red filled circle) samples as a function of galactic latitude  $b$  for  $|l| < 5^\circ$ . The subfields are combined into bins of width  $\Delta b = 0.5^\circ$ . The binned values are listed in Table 5 and 6. The filled circles, triangles and squares indicate  $\tau$  for all-source samples measured by MOA-II (this work), MOA-I and MACHO surveys, respectively. The red circles, open squares, circles and triangles denote the  $\tau$  for RCG samples by the MOA-II (this work), MACHO, OGLE-II and EROS surveys, respectively. The black and red solid lines indicate the best fit exponential functions for the MOA-II measurements. The red dashed line denote the best linear model for the OGLE-II RCG sample as a comparison.

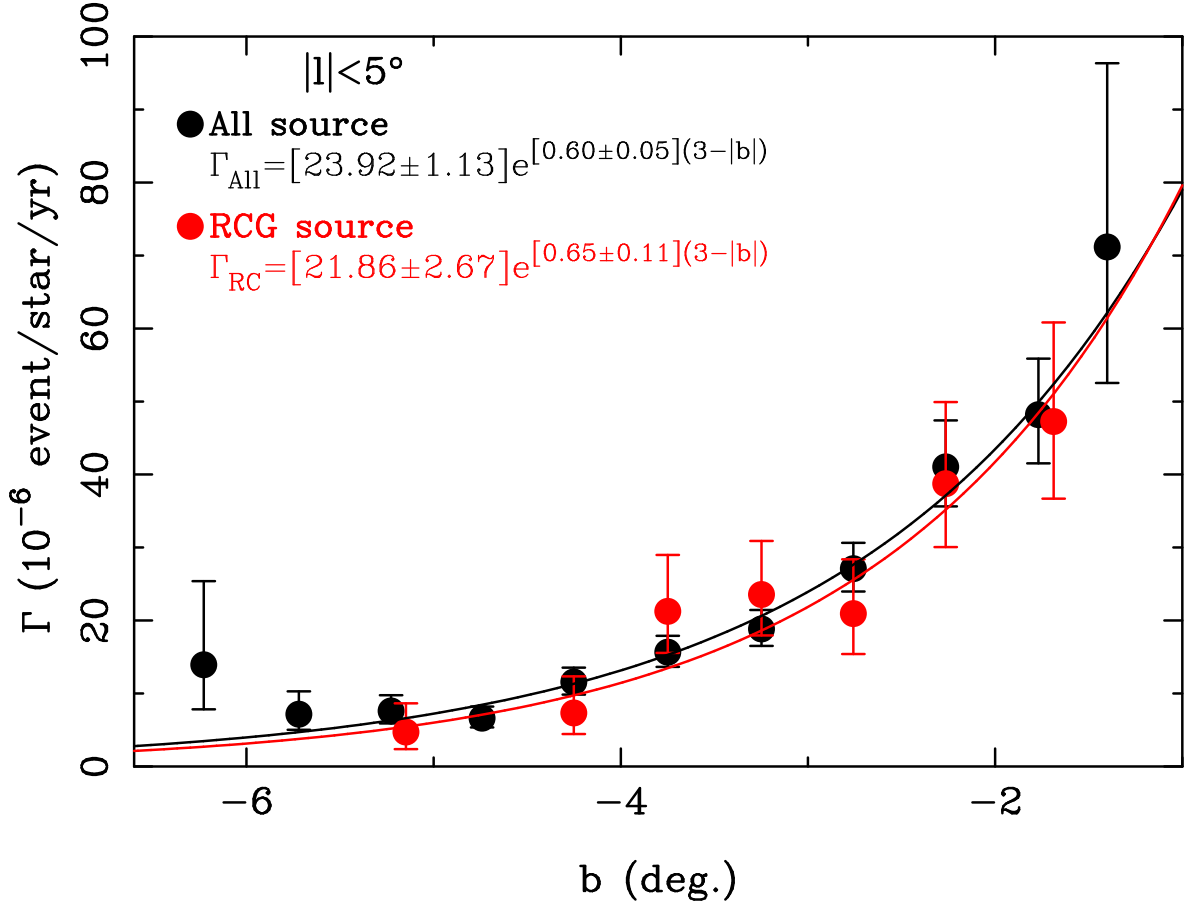


Fig. 6.—: The event rate per star per year,  $\Gamma$ , for the all-source (black) and RCG (red) samples as a function of the galactic latitude  $b$  for  $|l| < 5^\circ$ . The subfields are combined into bins of width  $\Delta b = 0.5^\circ$  for display purposes only, as the fitting was done using the unbinned subfield data with the Poisson statistics fitting method. The plotted values are listed in Tables 5 and 6. The black and red solid lines indicate the best fit exponential functions for the all-source and RCG samples, respectively.

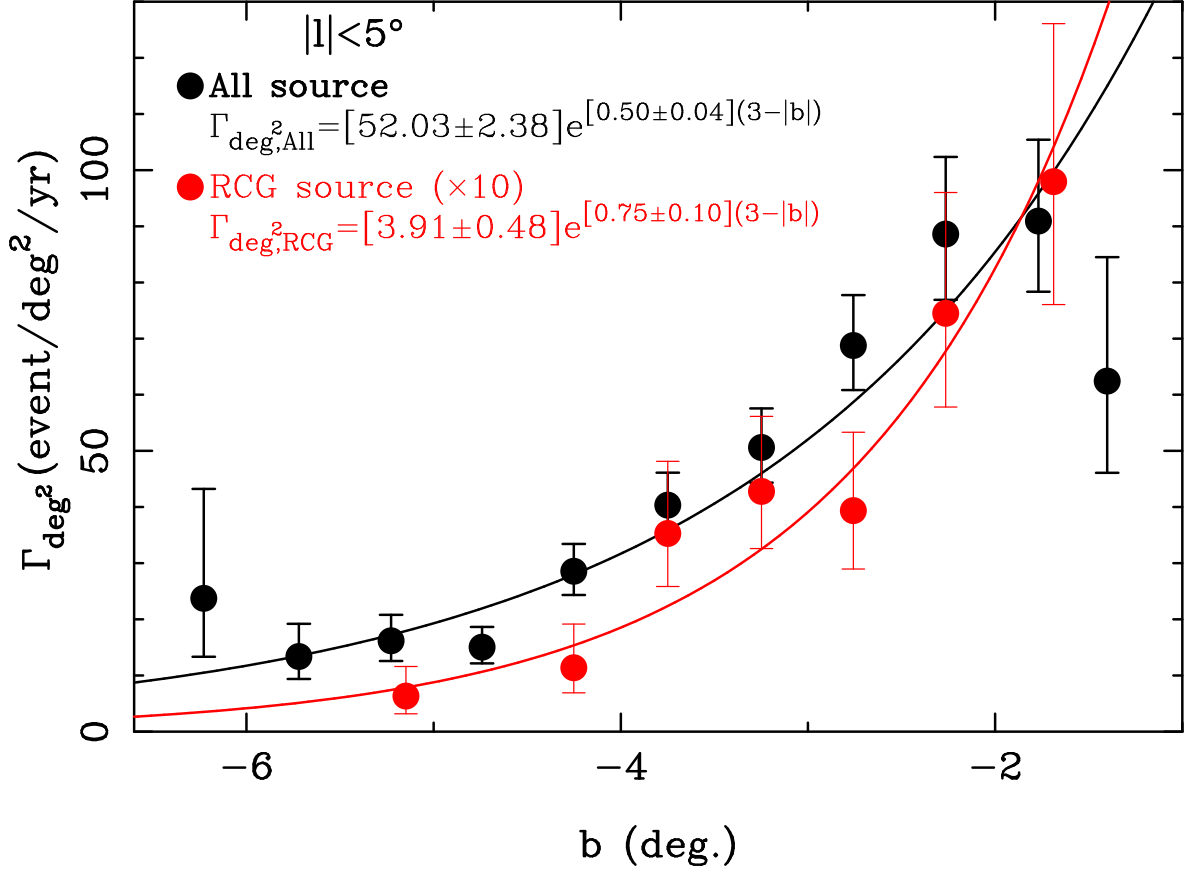


Fig. 7.—: The event rate per square degree per year,  $\Gamma_{\text{deg}^2}$ , for the all-source (black) and RCG (red) samples as a function of the galactic latitude  $b$  for  $|l| < 5^\circ$ . The subfields are combined into bins of width  $\Delta b = 0.5^\circ$  for display purposes only, as the fitting was done using the unbinned subfield data with the Poisson statistics fitting method. The plotted values are listed in Tables 5 and 6. The black and red solid lines indicate the best fit exponential functions for all sources and RCG sample, respectively.

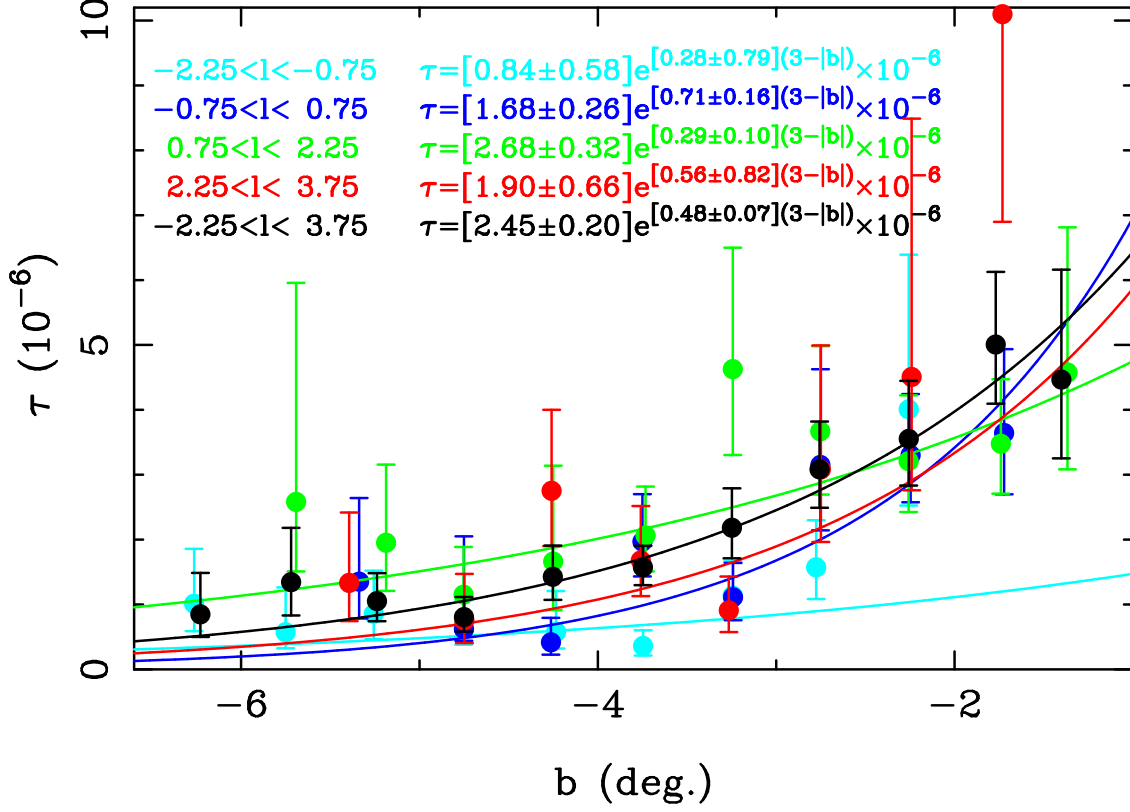


Fig. 8.—: The optical depth for events with  $t_E < 200$  days,  $\tau_{200}$ , for the all-source sample as a function of the galactic latitude  $b$  for different bins in Galactic longitude,  $l$ . The curves show the best exponential fit in  $b$ . The black curve is the fit to all the events with  $-2^\circ.25 < l < 3^\circ.75$ , and it provides a reasonable fit to all the longitude bins, except the  $0^\circ.75 < l < 2^\circ.25$  bin, where there is an enhancement to the rate.



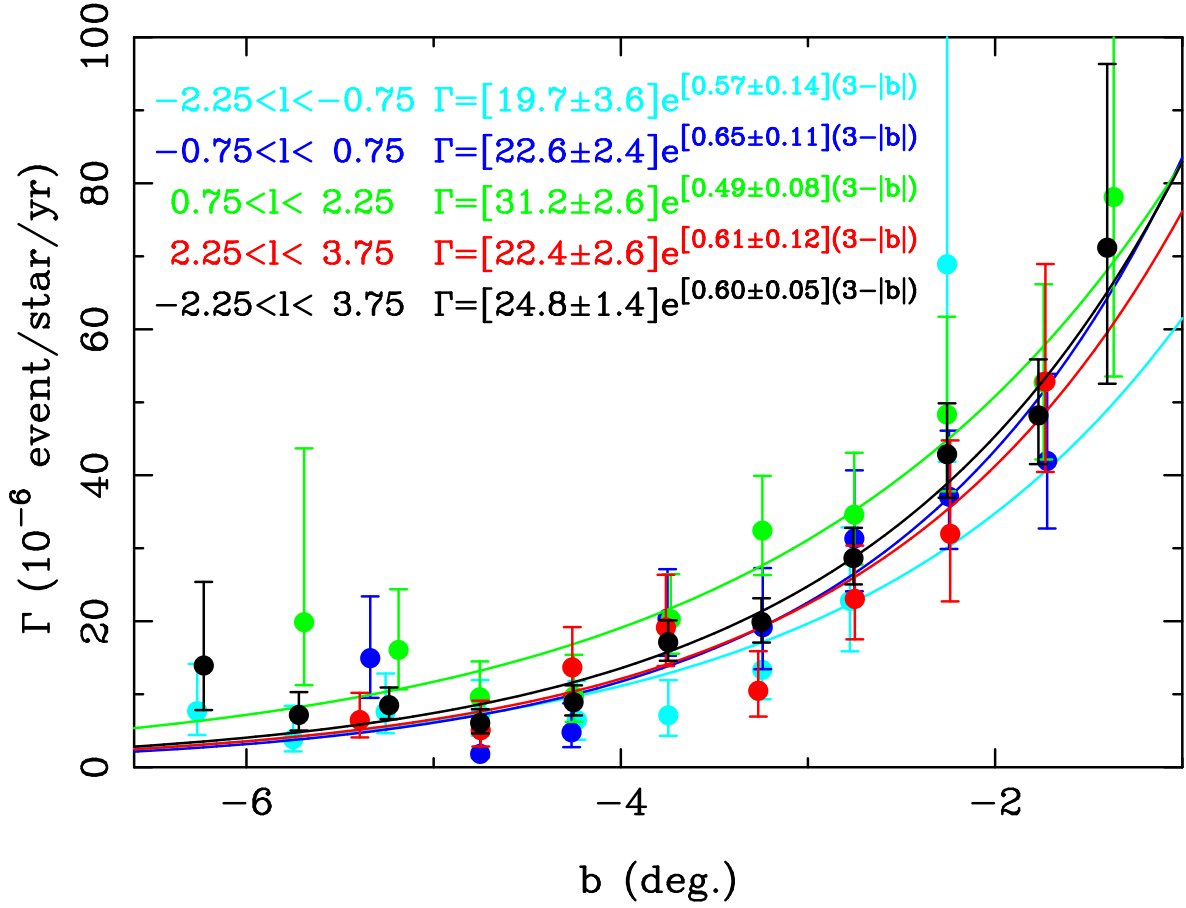


Fig. 9.—: The event rate per star per year,  $\Gamma$ , for the all-source sample as a function of the galactic latitude  $b$  for different bins in Galactic longitude,  $l$ . The curves show the best exponential fit in  $b$  to the unbinned subfield data. The black curve is the fit to all the events with  $-2^\circ.25 < l < 3^\circ.75$ , and it provides a reasonable fit to all the longitude bins, except the  $0^\circ.75 < l < 2^\circ.25$  bin, where there is an enhancement to the rate.

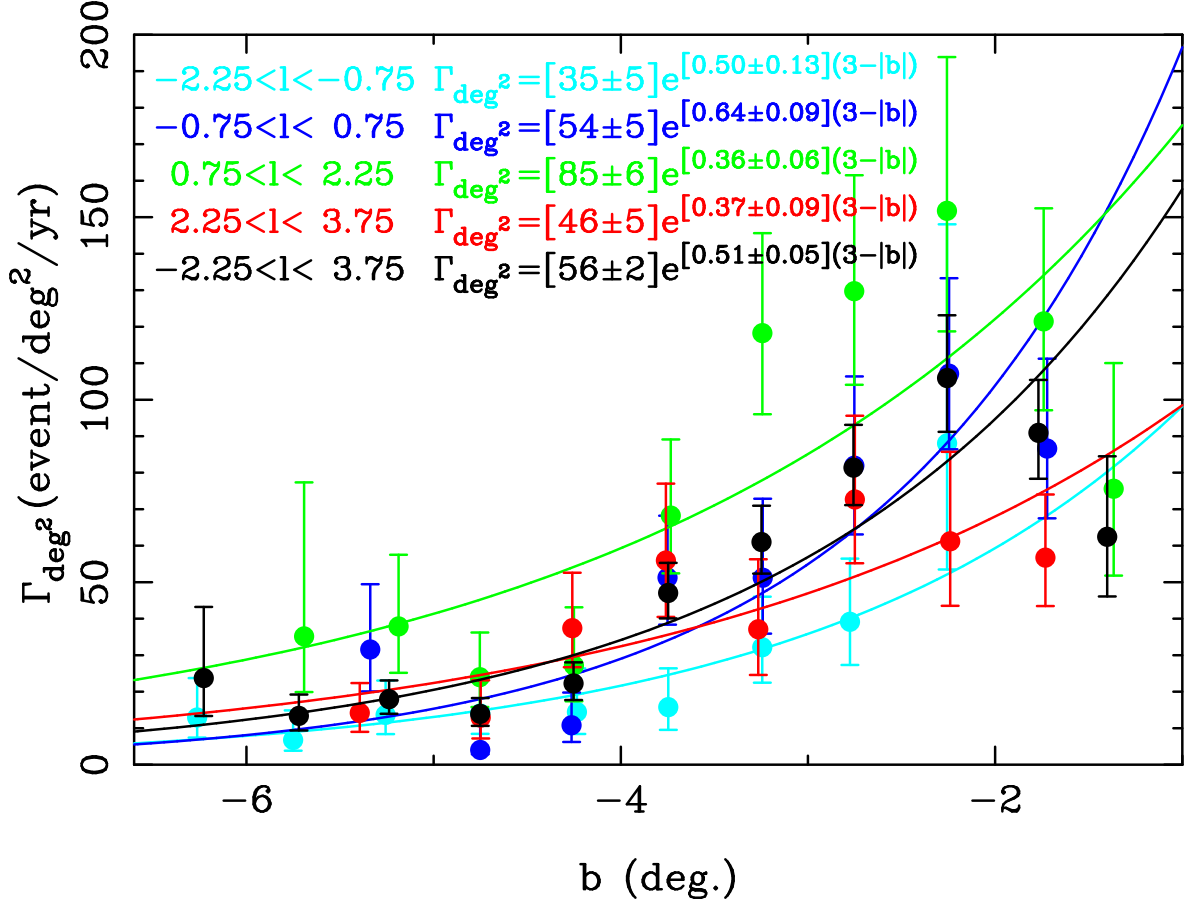


Fig. 10.—: The event rate per square degree per year,  $\Gamma_{\text{deg}^2}$ , for the all-source sample as a function of the galactic latitude  $b$  for different bins in Galactic longitude,  $l$ . The curves show the best exponential fit in  $b$  to the unbinned subfield data. The black curve is the fit to all the events with  $-2.25 < l < 3.75$ . The decline at  $l > -2^\circ$  is due to the high extinction.

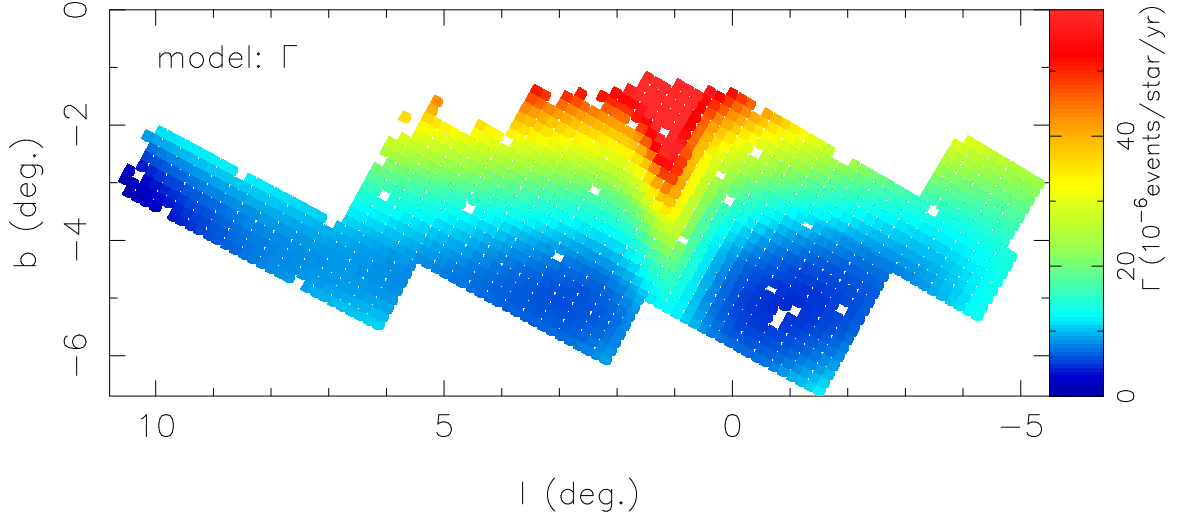


Fig. 11.—: A 16-parameter model of microlensing event rate per star for the all-source sample. The model is described by Equation (9) with parameters given in Table 8.

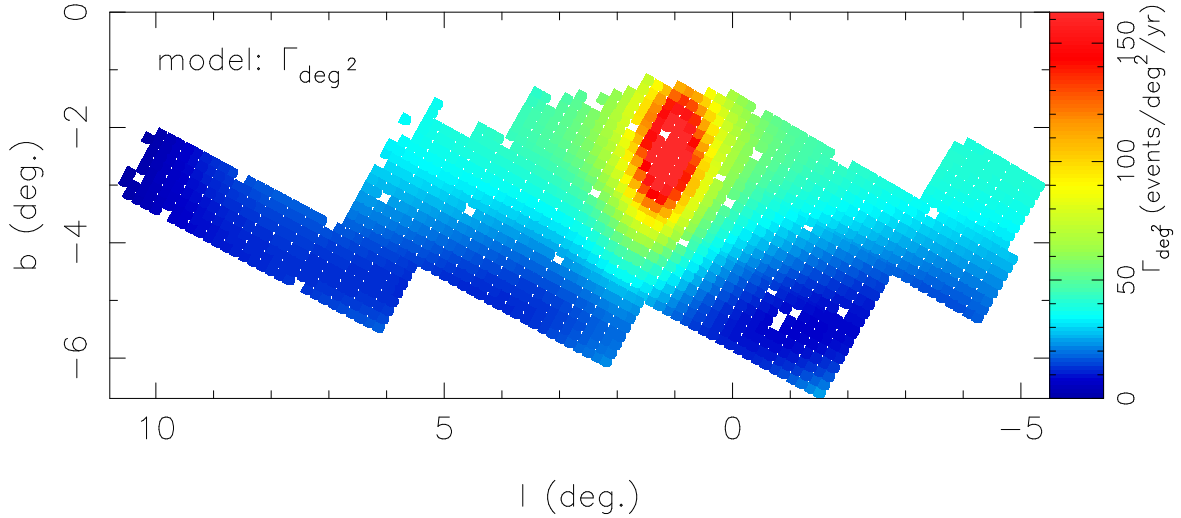


Fig. 12.—: A 16-parameter model of microlensing event rate per square degree for the all-source sample with  $I_s \leq 20$  mag. The model is described by Equation (9) with parameters given in Table 8.

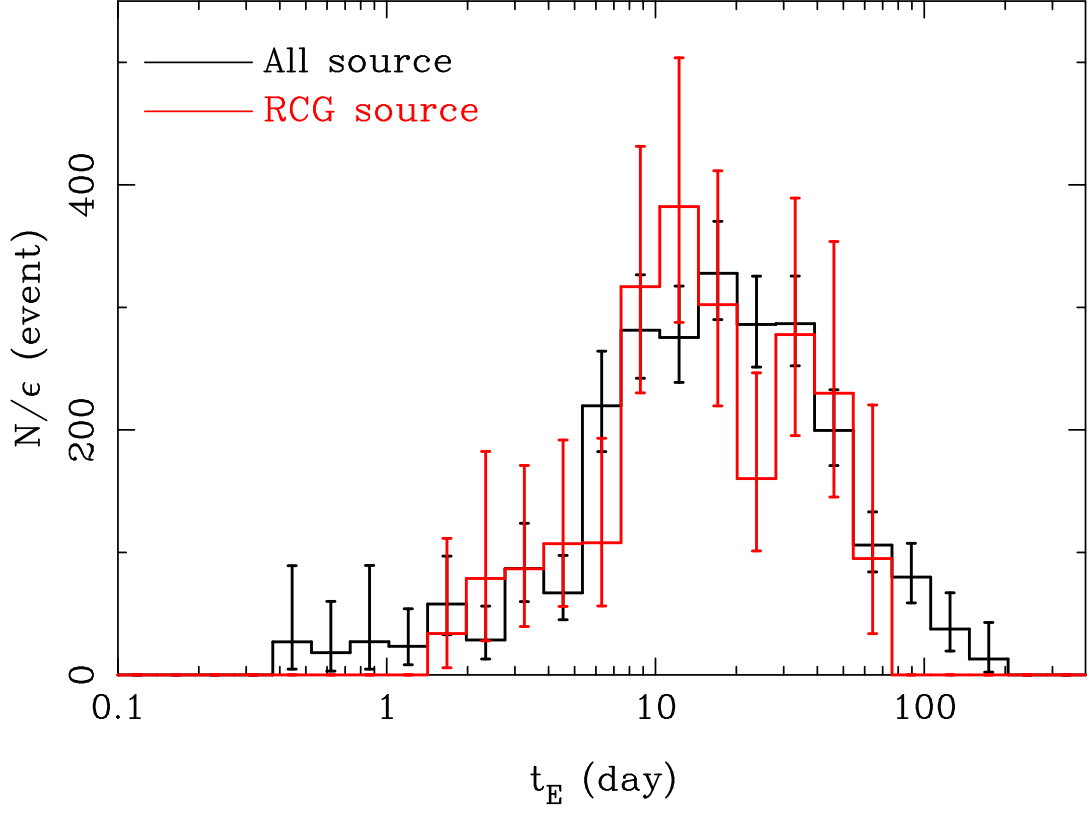


Fig. 13.—: The efficiency corrected Einstein radius crossing time distribution for the all-source sample in black and the RCG sample in red. The RCG  $t_E$  distribution has been scaled to mach the amplitude of the all-source sample.

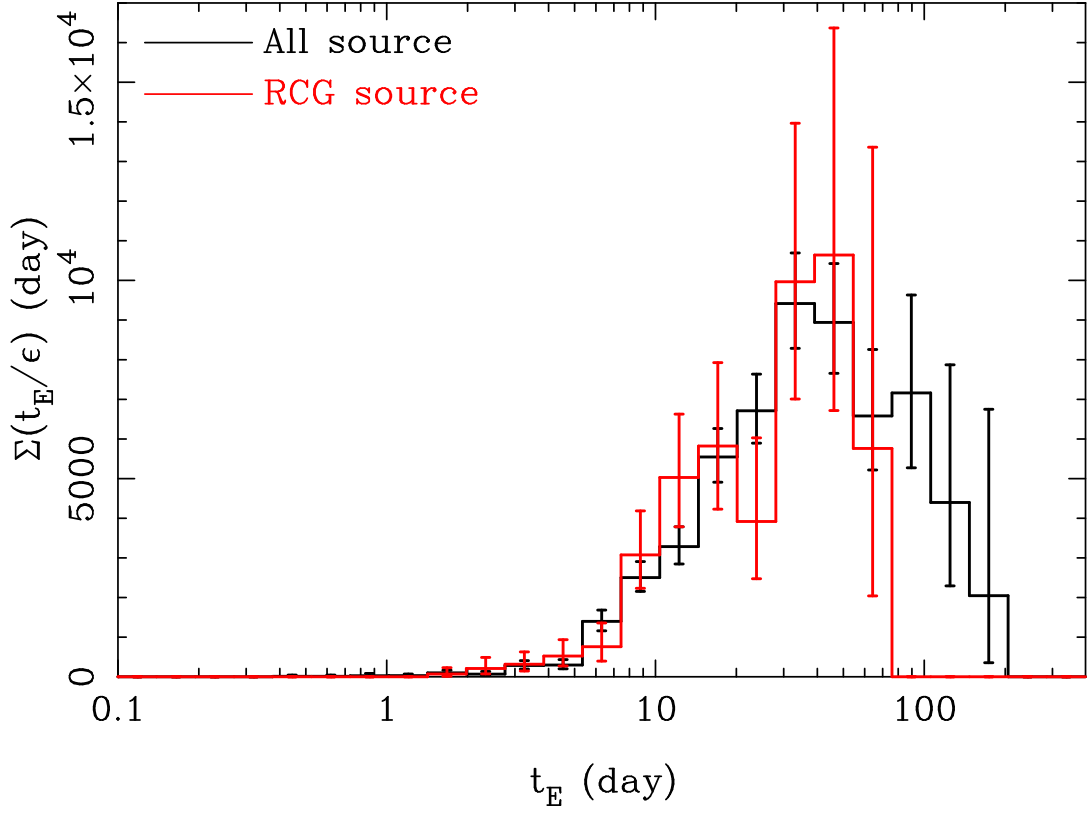


Fig. 14.—: The efficiency corrected Einstein radius crossing time distribution, weighted by the  $t_E$  values, for the all-source sample in black and RCG sample in red. This histogram indicates the contribution to the microlensing optical depth from each  $t_E$  bin. The amplitude of the RCG distribution has been scaled to match the amplitude for the all-source distribution.

Table 1. MOA-II Galactic bulge fields with Galactic coordinates of the mean field center ( $\langle l \rangle$ ,  $\langle b \rangle$ ), the number of subfields used ( $N_{\text{sub}}$ ), the number of frames ( $N_f$ ), the number of source stars ( $N_s$  in thousands), the number of microlensing events ( $N_{\text{ev}}$ ), the microlensing event rate per star per year ( $\Gamma$ ), the microlensing event rate per square degree per year ( $\Gamma_{\text{deg}^2}$ ), the optical depth ( $\tau_{200}$ ), and the mean detection efficiency weighted  $t_E$ .

Field	$\langle l \rangle$ ( $^\circ$ )	$\langle b \rangle$ ( $^\circ$ )	$N_{\text{sub}}$	$N_f$	$N_s$ ( $10^3$ )	$N_{\text{ev}}$	$\tau_{200}$ ( $10^{-6}$ )	$\Gamma(10^{-6})$ ( $\text{star}^{-1}\text{yr}^{-1}$ )	$\Gamma_{\text{deg}^2}$ ( $\text{deg.}^{-2}\text{yr}^{-1}$ )	$\langle t_E \rangle$ (day)
gb1	-4.3306	-3.1119	79	2253	4240	22	$2.56^{+1.93}_{-0.87}$	$19.0^{+5.3}_{-4.2}$	$37.0^{+10.4}_{-8.1}$	30.6
gb2	-3.8624	-4.3936	79	2386	4741	17	$0.94^{+0.29}_{-0.22}$	$11.3^{+3.2}_{-2.5}$	$24.7^{+6.9}_{-5.4}$	18.8
gb3	-2.3463	-3.5133	79	2067	4589	19	$1.31^{+0.42}_{-0.31}$	$11.1^{+2.9}_{-2.3}$	$23.5^{+6.2}_{-4.8}$	26.7
gb4	-0.8210	-2.6317	77	2985	4239	41	$3.00^{+0.75}_{-0.59}$	$35.1^{+7.3}_{-5.9}$	$70.2^{+14.7}_{-11.9}$	19.4
gb5	0.6544	-1.8595	65	8229	4457	67	$3.85^{+0.61}_{-0.53}$	$50.1^{+6.7}_{-6.1}$	$124.9^{+16.7}_{-15.1}$	17.4
gb6	1.8405	-1.4890	11	1779	317	4	$1.94^{+1.32}_{-0.76}$	$26.0^{+17.4}_{-10.4}$	$27.3^{+18.2}_{-10.9}$	16.9
gb7	-1.7147	-4.5992	78	1970	4404	15	$0.81^{+0.29}_{-0.21}$	$9.7^{+2.9}_{-2.3}$	$20.0^{+6.1}_{-4.6}$	18.8
gb8	-0.1937	-3.7495	78	2139	5244	16	$0.87^{+0.27}_{-0.21}$	$9.0^{+2.6}_{-2.0}$	$22.1^{+6.3}_{-4.9}$	21.7
gb9	1.3329	-2.8786	79	8301	7690	74	$3.33^{+0.60}_{-0.50}$	$34.0^{+4.5}_{-4.0}$	$120.4^{+15.9}_{-14.0}$	22.2
gb10	2.8448	-2.0903	70	1992	3707	36	$4.84^{+1.65}_{-1.23}$	$38.8^{+8.6}_{-6.9}$	$74.6^{+16.6}_{-13.3}$	28.3
gb11	-1.1093	-5.7257	76	2004	3728	8	$0.47^{+0.22}_{-0.15}$	$6.3^{+3.2}_{-2.1}$	$11.3^{+5.7}_{-3.8}$	16.9
gb12	0.4391	-4.8658	79	1790	4861	12	$1.06^{+0.49}_{-0.34}$	$7.2^{+2.4}_{-1.8}$	$16.2^{+5.4}_{-4.1}$	33.2
gb13	1.9751	-4.0190	79	1811	6793	27	$2.11^{+0.77}_{-0.58}$	$16.2^{+3.7}_{-3.0}$	$50.7^{+11.5}_{-9.3}$	29.6
gb14	3.5083	-3.1698	79	1770	6304	29	$1.98^{+0.72}_{-0.53}$	$17.6^{+3.7}_{-3.0}$	$51.2^{+10.8}_{-8.8}$	25.5
gb15	4.9940	-2.4496	62	1952	1872	14	$2.32^{+0.83}_{-0.61}$	$22.4^{+7.0}_{-5.3}$	$24.6^{+7.6}_{-5.8}$	23.5
gb16	2.6048	-5.1681	79	1756	5043	17	$1.56^{+0.56}_{-0.42}$	$10.0^{+2.8}_{-2.2}$	$23.3^{+6.5}_{-5.1}$	35.3
gb17	4.1498	-4.3365	79	1792	5513	16	$1.34^{+0.48}_{-0.35}$	$9.6^{+2.8}_{-2.2}$	$24.3^{+7.1}_{-5.5}$	31.7
gb18	5.6867	-3.5055	78	1799	3841	13	$1.01^{+0.41}_{-0.29}$	$9.5^{+3.1}_{-2.4}$	$17.1^{+5.6}_{-4.3}$	23.9
gb19	6.5534	-4.5749	78	1704	3838	12	$1.08^{+0.42}_{-0.30}$	$8.1^{+2.7}_{-2.0}$	$14.6^{+4.9}_{-3.7}$	30.0
gb20	8.1025	-3.7531	79	1679	3037	12	$1.17^{+0.44}_{-0.32}$	$10.8^{+3.6}_{-2.7}$	$15.1^{+5.0}_{-3.8}$	24.6
gb21	9.6172	-2.9318	73	1659	1896	3	$0.34^{+0.26}_{-0.16}$	$4.5^{+3.3}_{-2.1}$	$4.2^{+3.1}_{-2.0}$	17.0
all	1.8530	-3.6890	1536	—	90366	474	$1.87^{+0.15}_{-0.13}$	$17.7^{+0.9}_{-0.9}$	$37.8^{+1.9}_{-1.9}$	24.0
all* <sub>RC</sub>	1.8530	-3.6890	1536	—	6485	83	$1.58^{+0.27}_{-0.23}$	$18.7^{+2.2}_{-2.0}$	$2.9^{+0.3}_{-0.3}$	19.2

Note. — The values are for the all-source sample except for all<sub>RCG</sub> which is for the RCG source sample.

Table 2. MOA-II subfields with Galactic coordinates, the numbers of source stars and events, and the mean timescale and efficiencies for the all-source sample.

subfield	$l$ ( $^{\circ}$ )	$b$ ( $^{\circ}$ )	$N_s$	$N_{ev}$	$\langle t_E \rangle$ (days)	$\langle \varepsilon \rangle$
gb5-1-3	1.1704	-1.3459	24032	2	15.4	0.2054
gb5-1-7	1.3125	-1.2630	25504	1	15.4	0.2058
gb5-2-2	0.7835	-1.3776	29267	1	15.5	0.1911
gb5-2-3	0.8685	-1.5224	72017	0	15.4	0.1902
gb5-2-6	0.9280	-1.2935	20980	0	15.2	0.1905
gb5-2-7	1.0130	-1.4379	61885	1	15.2	0.1902
gb5-3-1	0.3942	-1.4104	23886	0	17.6	0.1981
gb5-3-2	0.4788	-1.5549	31046	0	17.4	0.1968
gb5-3-3	0.5639	-1.6998	66763	1	16.8	0.1951
gb5-3-6	0.6239	-1.4697	43697	2	16.3	0.1953
gb5-3-7	0.7091	-1.6146	83169	1	15.9	0.1941
gb5-4-0	0.0089	-1.4439	39811	0	19.8	0.1910
gb5-4-1	0.0918	-1.5877	51173	0	20.3	0.1916
gb5-4-2	0.1755	-1.7322	74557	1	20.7	0.1912
gb5-4-3	0.2599	-1.8771	96247	1	20.3	0.1898
gb5-4-5	0.2356	-1.5028	27844	0	19.1	0.1899
gb5-4-6	0.3197	-1.6474	42434	2	18.9	0.1890
gb5-4-7	0.4044	-1.7925	56646	3	18.6	0.1874
gb5-5-0	-0.2872	-1.6227	37610	1	20.4	0.1910
gb5-5-1	-0.2055	-1.7661	39203	0	21.9	0.1932
gb5-5-2	-0.1227	-1.9100	82900	0	22.8	0.1939

Note. —  $N_s$  and  $N_{ev}$  indicate the numbers of stars and microlensing events down to  $I_s < 20$  mag. The mean timescales,  $\langle t_E \rangle$ , are averaged over subfields within  $1^{\circ}$  from the center of each subfield using a Gaussian weighting function with  $\sigma = 0^{\circ}.4$ .  $\langle \varepsilon \rangle$  is average detection efficiency for the subfields by using the  $t_E$  distribution in the the subfields within  $1^{\circ}$  from the center of each subfield. A complete electronic version of the table is available on the web.

Table 3. MOA-II subfields with Galactic coordinates, the numbers of source stars and events, and the mean timescale and efficiencies for the RCG sample.

subfield	$l$ ( $^{\circ}$ )	$b$ ( $^{\circ}$ )	$N_s$	$N_{\text{ev}}$	$\langle t_E \rangle$ (days)	$\langle \varepsilon \rangle$
gb5-1-3	1.1704	-1.3459	5267	1	14.2	0.3363
gb5-1-7	1.3125	-1.2630	5419	0	13.9	0.3365
gb5-2-2	0.7835	-1.3776	5630	1	15.0	0.3673
gb5-2-3	0.8685	-1.5224	8184	0	15.1	0.3683
gb5-2-6	0.9280	-1.2935	4748	0	14.5	0.3670
gb5-2-7	1.0130	-1.4379	7803	0	14.6	0.3684
gb5-3-1	0.3942	-1.4104	4769	0	16.3	0.3965
gb5-3-2	0.4788	-1.5549	5869	0	16.2	0.3974
gb5-3-3	0.5639	-1.6998	7452	0	16.3	0.3984
gb5-3-6	0.6239	-1.4697	6826	0	15.6	0.3974
gb5-3-7	0.7091	-1.6146	7526	0	15.7	0.3986
gb5-4-0	0.0089	-1.4439	6872	0	17.6	0.3784
gb5-4-1	0.0918	-1.5877	7065	0	17.6	0.3784
gb5-4-2	0.1755	-1.7322	7435	1	17.5	0.3787
gb5-4-3	0.2599	-1.8771	7315	0	17.4	0.3790
gb5-4-5	0.2356	-1.5028	5914	0	17.0	0.3785
gb5-4-6	0.3197	-1.6474	6266	0	16.9	0.3788
gb5-4-7	0.4044	-1.7925	7070	1	16.9	0.3792
gb5-5-0	-0.2872	-1.6227	6417	0	18.7	0.4131
gb5-5-1	-0.2055	-1.7661	6684	0	18.6	0.4131
gb5-5-2	-0.1227	-1.9100	7564	0	18.5	0.4133

Note. — Notation is the same as Table 2, but for the RCG sample. A complete electronic version of the table is available on the web.



Table 4. Microlensing events used in the optical depth and event rate measurements.

ID	R.A. (2000)	Dec. (2000)	$N_{\text{data}}$	$t_0$ (JD')	$t_E$ (day)	$u_0$	$I_s$ (mag)	$\frac{\chi^2}{dof}$
gb1-R-1-14	17:45:11.248	-33:38:54.84	2052	3828.94193	23.60±2.28	0.909150±0.144886	16.8	0.99
gb1-R-1-52516	17:45:46.378	-33:36:05.22	2073	4031.68805	23.02±0.73	0.090750±0.003734	18.1	1.58
gb1-R-2-22735	17:45:35.960	-33:45:56.56	2074	3883.90740	22.39±0.39	0.212003±0.005573	18.0	0.67
gb1-R-3-64176	17:44:52.898	-34:21:36.52	2092	4193.71721	10.64±0.14	0.766208±0.015656	14.9	1.20
gb1-R-3-76	17:45:40.324	-34:20:04.75	2106	3825.27275	157.57±11.00	0.188031±0.020548	19.7	0.87
gb1-R-3-46605	17:45:24.278	-34:05:15.32	2088	4001.26676	16.60±1.18	0.173574±0.043284	18.6	0.89
gb1-R-4-47848	17:45:45.039	-34:27:53.52	2103	4303.16456	14.98±1.14	0.331496±0.041186	19.5	0.84
gb1-R-4-18284	17:46:24.506	-34:30:36.82	2101	3883.24171	0.73±0.08	0.028096±0.003360	19.7	0.77
gb1-R-4-910	17:46:53.887	-34:30:42.59	2095	3887.62778	26.14±1.06	0.587581±0.038963	17.7	0.68
gb1-R-5-65454	17:45:22.188	-34:57:04.75	2075	4221.40839	40.11±0.45	0.190260±0.002905	17.5	1.66
gb1-R-5-82191	17:46:01.446	-34:54:35.01	2089	4312.71403	14.23±0.41	0.106859±0.004776	19.2	1.31
gb1-R-6-77689	17:50:28.442	-34:49:23.09	2068	4364.59588	45.51±0.74	0.413738±0.010909	17.1	1.30
gb1-R-6-82519	17:50:05.385	-34:51:36.71	2073	4362.33309	3.26±0.54	0.840722±0.290765	17.1	1.51
gb1-R-6-79294	17:49:50.655	-34:53:49.40	2063	4340.06886	23.06±0.94	0.375246±0.023845	18.7	0.77
gb1-R-6-65555	17:47:53.567	-34:50:55.15	2076	4241.08796	4.92±0.32	0.050412±0.004092	19.4	1.48
gb1-R-6-40898	17:49:46.072	-35:05:13.00	2061	4019.80173	11.24±0.69	0.475032±0.049014	17.6	0.73
gb1-R-6-73986	17:48:11.363	-35:02:34.80	2081	4291.58993	19.18±0.70	0.153344±0.007234	19.6	0.76
gb1-R-7-71783	17:50:17.617	-34:27:00.09	2075	4303.67369	30.97±2.54	0.464778±0.054527	19.3	1.06
gb1-R-7-30409	17:47:53.653	-34:29:04.26	2062	3953.51717	12.43±1.16	0.810060±0.140936	17.8	0.65

Note. — The error bars for  $t_E$  and  $u_0$  indicate 68% confidence intervals.  $\text{JD}' = \text{JD} - 2450000$ .  $I_s$  indicates the best fit  $I$ -band source magnitude.  $\chi^2/dof$  is the reduced chi-square for the best fit single-lens model. The complete table is available electronically on the ApJ website. The print edition contains only a sample.

Table 5. Microlensing optical depth and event rates binned in  $b$  for the all-source sample with  $|l| < 5^\circ$ .

$\langle b \rangle^*$ ( $^\circ$ )	$N_{\text{sub}}$	$N_s$	$N_{\text{ev}}$	$\tau(10^{-6})$	$\Gamma(10^{-6})$ ( $\text{star}^{-1} \text{ yr}^{-1}$ )	$\Gamma_{\text{deg}^2}$ ( $\text{deg.}^{-2} \text{ yr}^{-1}$ )
-1.4012	20	482422	12	$4.47^{+1.69}_{-1.21}$	$71.2^{+25.2}_{-18.6}$	$62.4^{+22.1}_{-16.3}$
-1.7690	70	3631956	52	$5.01^{+1.12}_{-0.91}$	$48.2^{+7.7}_{-6.7}$	$90.9^{+14.5}_{-12.6}$
-2.2645	114	6766400	70	$3.49^{+0.81}_{-0.66}$	$41.1^{+6.4}_{-5.4}$	$88.6^{+13.7}_{-11.7}$
-2.7576	146	10190175	75	$3.33^{+0.88}_{-0.69}$	$27.1^{+3.5}_{-3.1}$	$68.8^{+9.0}_{-7.9}$
-3.2486	168	12407499	67	$1.88^{+0.43}_{-0.35}$	$18.8^{+2.6}_{-2.3}$	$50.6^{+7.0}_{-6.3}$
-3.7490	172	12182546	58	$1.52^{+0.26}_{-0.23}$	$15.7^{+2.2}_{-2.0}$	$40.3^{+5.8}_{-5.2}$
-4.2512	172	11677303	43	$1.47^{+0.32}_{-0.26}$	$11.6^{+2.0}_{-1.7}$	$28.6^{+4.9}_{-4.2}$
-4.7410	154	9620731	22	$0.76^{+0.22}_{-0.18}$	$6.6^{+1.6}_{-1.3}$	$15.0^{+3.6}_{-2.9}$
-5.2270	101	5911839	16	$0.94^{+0.39}_{-0.28}$	$7.6^{+2.2}_{-1.7}$	$16.2^{+4.6}_{-3.6}$
-5.7197	56	2874105	8	$1.34^{+0.84}_{-0.51}$	$7.2^{+3.1}_{-2.1}$	$13.4^{+5.8}_{-4.0}$
-6.2282	21	983156	4	$0.85^{+0.64}_{-0.35}$	$13.9^{+11.5}_{-6.1}$	$23.7^{+19.5}_{-10.4}$

Note. — \*Average galactic latitude of fields in each bin.  $N_{\text{sub}}$ ,  $N_s$  and  $N_{\text{ev}}$  indicate the number of subfields, source stars and microlensing events in each bin.

Table 6. Microlensing optical depth and event rates binned in  $b$  for the RCG sample with  $|l| < 5^\circ$ .

$\langle b \rangle^*$ ( $^\circ$ )	$N_{\text{sub}}$	$N_s$	$N_{\text{ev}}$	$\tau(10^{-6})$	$\Gamma(10^{-6})$ ( $\text{star}^{-1} \text{ yr}^{-1}$ )	$\Gamma_{\text{deg}^2}$ ( $\text{deg.}^{-2} \text{ yr}^{-1}$ )
-1.6872	90	512987	16	$2.87^{+1.03}_{-0.75}$	$47.3^{+13.6}_{-10.6}$	$9.8^{+2.8}_{-2.2}$
-2.2645	114	602968	16	$3.44^{+1.45}_{-1.03}$	$38.7^{+11.2}_{-8.7}$	$7.5^{+2.2}_{-1.7}$
-2.7576	146	754360	11	$1.40^{+0.67}_{-0.45}$	$20.9^{+7.4}_{-5.5}$	$3.9^{+1.4}_{-1.0}$
-3.2486	168	839277	14	$1.93^{+0.76}_{-0.55}$	$23.6^{+7.3}_{-5.6}$	$4.3^{+1.3}_{-1.0}$
-3.7490	172	785581	11	$1.95^{+0.98}_{-0.64}$	$21.2^{+7.7}_{-5.7}$	$3.5^{+1.3}_{-0.9}$
-4.2512	172	734458	4	$0.57^{+0.55}_{-0.26}$	$7.3^{+5.0}_{-2.9}$	$1.1^{+0.8}_{-0.4}$
-5.1480	332	1225445	3	$0.93^{+0.99}_{-0.41}$	$4.7^{+3.9}_{-2.4}$	$0.6^{+0.5}_{-0.3}$

Note. — \*Average galactic latitude of fields in each bin. The notation is the same as in Table 5.

Table 7. Average microlensing optical depth and event rates at the position of each subfield for the all-source sample.

subfield	$l$ ( $^{\circ}$ )	$b$ ( $^{\circ}$ )	$N_{\text{sub}}$	$N_s$	$N_{\text{ev}}$	$\tau(10^{-6})$	$\Gamma(10^{-6})$ ( $\text{star}^{-1}\text{yr}^{-1}$ )	$\Gamma_{\text{deg}^2}$ ( $\text{deg.}^{-2}\text{yr}^{-1}$ )
gb5-1-3	1.1704	-1.3459	58	3476887	55	$4.0^{+0.8}_{-0.7}$	$59.3^{+16.9}_{-13.4}$	$109.0^{+31.1}_{-24.7}$
gb5-1-7	1.3125	-1.2630	51	2826886	46	$4.0^{+0.9}_{-0.8}$	$59.4^{+20.2}_{-14.4}$	$96.6^{+32.8}_{-23.3}$
gb5-2-2	0.7835	-1.3776	59	3756406	59	$3.8^{+0.7}_{-0.6}$	$56.1^{+15.4}_{-11.9}$	$118.0^{+32.4}_{-25.1}$
gb5-2-3	0.8685	-1.5224	69	4605788	67	$3.8^{+0.7}_{-0.6}$	$55.8^{+12.9}_{-10.3}$	$126.1^{+29.2}_{-23.3}$
gb5-2-6	0.9280	-1.2935	54	3210920	49	$3.9^{+0.8}_{-0.7}$	$58.4^{+17.6}_{-13.3}$	$112.9^{+33.9}_{-25.7}$
gb5-2-7	1.0130	-1.4379	63	4042440	63	$3.9^{+0.7}_{-0.6}$	$58.1^{+14.6}_{-11.4}$	$120.2^{+30.2}_{-23.7}$
gb5-3-1	0.3942	-1.4104	53	3639406	52	$3.7^{+0.8}_{-0.6}$	$47.6^{+14.9}_{-11.3}$	$103.0^{+32.2}_{-24.5}$
gb5-3-2	0.4788	-1.5549	67	4635780	63	$3.7^{+0.7}_{-0.6}$	$48.5^{+12.0}_{-9.5}$	$114.3^{+28.4}_{-22.3}$
gb5-3-3	0.5639	-1.6998	78	5615435	74	$3.7^{+0.6}_{-0.5}$	$49.4^{+10.7}_{-8.9}$	$126.2^{+27.4}_{-22.6}$
gb5-3-6	0.6239	-1.4697	65	4326789	65	$3.8^{+0.7}_{-0.6}$	$52.4^{+13.7}_{-10.6}$	$117.9^{+30.8}_{-23.9}$
gb5-3-7	0.7091	-1.6146	76	5229492	75	$3.7^{+0.6}_{-0.5}$	$53.0^{+11.7}_{-9.3}$	$128.6^{+28.4}_{-22.6}$
gb5-4-0	0.0089	-1.4439	48	3061436	37	$3.5^{+0.9}_{-0.7}$	$39.9^{+14.7}_{-11.1}$	$82.1^{+30.2}_{-22.8}$
gb5-4-1	0.0918	-1.5877	59	3949695	52	$3.7^{+0.9}_{-0.7}$	$40.9^{+12.1}_{-9.1}$	$92.6^{+27.5}_{-20.6}$
gb5-4-2	0.1755	-1.7322	73	5041433	65	$3.8^{+0.8}_{-0.7}$	$41.9^{+10.2}_{-8.4}$	$104.0^{+25.4}_{-20.8}$
gb5-4-3	0.2599	-1.8771	81	5740732	70	$3.8^{+0.7}_{-0.6}$	$42.7^{+9.3}_{-7.5}$	$114.7^{+24.9}_{-20.2}$
gb5-4-5	0.2356	-1.5028	56	3878445	53	$3.7^{+0.8}_{-0.7}$	$43.6^{+13.1}_{-10.2}$	$97.5^{+29.2}_{-22.7}$
gb5-4-6	0.3197	-1.6474	70	4909533	67	$3.8^{+0.8}_{-0.6}$	$45.1^{+11.1}_{-8.8}$	$110.1^{+27.1}_{-21.4}$
gb5-4-7	0.4044	-1.7925	81	5774820	76	$3.8^{+0.7}_{-0.6}$	$46.1^{+10.1}_{-8.5}$	$121.9^{+26.7}_{-22.5}$
gb5-5-0	-0.2872	-1.6227	53	3233763	43	$3.6^{+0.9}_{-0.7}$	$40.1^{+16.4}_{-11.5}$	$81.0^{+33.2}_{-23.3}$
gb5-5-1	-0.2055	-1.7661	63	4002999	50	$3.8^{+0.9}_{-0.7}$	$39.3^{+13.0}_{-9.7}$	$86.8^{+28.8}_{-21.5}$
gb5-5-2	-0.1227	-1.9100	76	4986751	57	$3.9^{+0.9}_{-0.7}$	$38.7^{+11.5}_{-8.7}$	$93.1^{+27.7}_{-21.0}$

Note. — The averages include all the subfields within  $1^{\circ}$  of the center of each subfield with a Gaussian weighting function with  $\sigma = 0^{\circ}.4$ .  $N_{\text{sub}}$ ,  $N_s$  and  $N_{\text{ev}}$  are numbers of subfields, source stars and microlensing events in this  $1^{\circ}$  circle, respectively. A complete electronic version of this table is available on the web.

Table 8. The best 2D model parameters for  $\Gamma$  and  $\Gamma_{\text{deg}^2}$ .

param	$\Gamma$	$\Gamma_{\text{deg}^2}$
$a_0$	93.032844	-24.481156
$a_1$	1.248177	5.539010
$a_2$	36.846116	-73.451537
$a_3$	-0.282139	-0.790312
$a_4$	0.405687	3.113193
$a_5$	4.142922	-24.290347
$a_6$	-0.025380	-0.020730
$a_7$	-0.124668	-0.244327
$a_8$	0.021965	0.370164
$a_9$	0.072898	-2.156637
$a_{10}$	0.337819	0.055451
$a_{11}$	-0.496257	-0.037629
$a_{12}$	0.035555	0.024214
$a_{13}$	0.218693	0.027694
$a_{14}$	-0.004649	0.009795
$a_{15}$	0.007841	0.007221

Note. — The model parameters are defined in Equation (9).